2014

Elvis: Exploring the Local Volume In Simulations

Shea Garrison-Kimmel
University of California - Irvine

Michael Boylan-Kolchin
University of California - Irvine

James S. Bullock
University of California - Irvine

Kyle Lee
Chapman University

Recommended Citation

Garrison-Kimmel, Shea, et al. "ELVIS: Exploring the Local Volume in Simulations." *Monthly Notices of the Royal Astronomical Society* 438.3 (2014): 2578-2596. doi: 10.1093/mnras/stt2377

Elvis: Exploring the Local Volume In Simulations

Monthly Notices of the ROYAL ASTRONOMICAL SOCIETY
MNRAS Advance Access published January 13, 2014
MNRAS (2014) doi:10.1093/mnras/stt2377

ELVIS: Exploring the Local Volume in Simulations

Shea Garrison-Kimmel,[1]★ Michael Boylan-Kolchin,[1,2] James S. Bullock[1] and Kyle Lee[3]

[1]*Center for Cosmology, Department of Physics and Astronomy, University of California, Irvine, CA 92697, USA*
[2]*Department of Astronomy and Joint Space-Science Institute, University of Maryland, College Park, MD 20742-2421, USA*
[3]*Chapman University, Orange, CA 92866, USA*

Accepted 2013 December 6. Received 2013 December 4; in original form 2013 October 24

ABSTRACT

We introduce a set of high-resolution dissipationless simulations that model the Local Group (LG) in a cosmological context: Exploring the Local Volume in Simulations (ELVIS). The suite contains 48 Galaxy-size haloes, each within high-resolution volumes that span 2–5 Mpc in size, and each resolving thousands of systems with masses below the atomic cooling limit. Half of the ELVIS galaxy haloes are in paired configurations similar to the Milky Way (MW) and M31; the other half are isolated, mass-matched analogues. We find no difference in the abundance or kinematics of substructure within the virial radii of isolated versus paired hosts. On Mpc scales, however, LG-like pairs average almost twice as many companions and the velocity field is kinematically hotter and more complex. We present a refined abundance matching relation between stellar mass and halo mass that reproduces the observed satellite stellar mass functions of the MW and M31 down to the regime where incompleteness is an issue, $M_* \sim 5 \times 10^5\,\mathrm{M}_\odot$. Within a larger region spanning approximately 3 Mpc, the same relation predicts that there should be ∼1000 galaxies with $M_* > 10^3\,\mathrm{M}_\odot$ awaiting discovery. We show that up to 50 per cent of haloes within 1 Mpc of the MW or M31 could be systems that have previously been within the virial radius of either giant. By associating never accreted haloes with gas-rich dwarfs, we show that there are plausibly 50 undiscovered dwarf galaxies with H I masses $>10^5\,\mathrm{M}_\odot$ within the local volume. The radial velocity distribution of these predicted gas-rich dwarfs can be used to inform follow-up searches based on ultracompact high-velocity clouds found in the ALFALFA survey.

Key words: galaxies: haloes – Local Group – cosmology: theory – dark matter.

1 INTRODUCTION

The Local Group (LG) provides an important test bed for theories of galaxy formation, both in its connection to small-scale probes of the consensus dark energy plus cold dark matter (ΛCDM) cosmological model (Klypin et al. 1999; Moore et al. 1999; Strigari et al. 2008; Boylan-Kolchin, Bullock & Kaplinghat 2011; Walker & Peñarrubia 2011; Arraki et al. 2012; Zolotov et al. 2012; Garrison-Kimmel et al. 2013) and as a potential hunting ground for the descendants of reionization and first light (Bullock, Kravtsov & Weinberg 2000; Ricotti & Gnedin 2005; Madau et al. 2008). The focus on these issues is well motivated: given inevitable completeness limitations, nearby galaxies offer our best avenue for characterizing the faint end of the global luminosity function and for studying resolved stellar populations as beacons from an earlier age (see, e.g. Makarov & Karachentsev 2011; Weisz et al. 2011; McConnachie 2012; Karachentsev & Kaisina 2013; Tully et al. 2013).

Numerical simulations have emerged as the most useful tool for making predictions about non-linear structures in ΛCDM. While simulations of cosmologically large volumes enable statistical comparisons with a variety of observations (e.g. Davis et al. 1985; Gross et al. 1998; Springel et al. 2005; Boylan-Kolchin et al. 2009; Klypin, Trujillo-Gomez & Primack 2011), cosmological zoom-in simulations are the de facto standard for the most detailed comparisons of individual objects. The zoom-in technique (Katz & White 1993; Oñorbe et al. 2014) focuses computational power on a small, high-resolution region nested within a lower resolution, cosmological-size volume, thereby retaining the large-scale, low-frequency cosmological modes important for convergence but also allowing for the high resolutions required to obtain a wide dynamic range.

Very high resolution zoom-in simulations of Milky Way (MW) mass haloes have been useful for making and testing predictions of the ΛCDM theory (e.g. Diemand et al. 2008; Kuhlen, Diemand

★ E-mail: sgarriso@uci.edu

& Madau 2008; Springel et al. 2008), often through comparisons to dwarf satellite galaxies of the LG (Koposov et al. 2009; Strigari, Frenk & White 2010; Boylan-Kolchin, Bullock & Kaplinghat 2012). However, in order to achieve the highest resolution possible, these simulations have concentrated on fairly isolated systems.[1] In reality, the MW is not isolated, but has a nearby companion of comparable luminosity, the Andromeda galaxy (M31). The existence of M31 at a distance of approximately 800 kpc from the MW implies that isolated zoom simulations cannot be used to faithfully make predictions for the local volume[2] beyond ∼400 kpc of either system. Furthermore, several simulations that have explored the role of LG-like environments in shaping galaxy properties have found evidence that the local configuration may even bias galaxy properties within each giant's virial radius compared to isolated counterparts (Gottloeber, Hoffman & Yepes 2010; Libeskind et al. 2010; Forero-Romero et al. 2011; Few et al. 2012).

Motivated by these concerns, here we introduce a set of dissipationless simulations designed to confront the local volume in a cosmological context. We call this project Exploring the Local Volume in Simulations (ELVIS). The simulation suite consists of 12 zoom-in regions of LG analogue halo pairs and 24 isolated haloes that are mass matched to create a control sample for those pairs. Below, we describe the selection of ELVIS pairs, their simulation details, and properties of the host haloes (Section 2). We investigate the environments that surround them in comparison to those of the control hosts as well as the dynamical histories of bound haloes around the ELVIS giants by characterizing the fraction of 'backsplash' haloes – systems that at one point had been within the virial radius of a giant – as a function of distance (Section 3). Finally, we compare number counts and kinematic properties of the subhaloes found in paired and isolated samples, and we use abundance matching (AM) to make predictions for the stellar and H I mass functions within the local volume (Section 4).

With the publication of this paper, we have publicly released all of the data in the ELVIS suite, including full merger trees, $z = 0$ halo catalogues and particle information.[3]

2 THE ELVIS SUITE

The ELVIS simulations were run using GADGET-3 and GADGET-2 (Springel 2005), both tree-based *N*-body codes. For the underlying cosmological model, we have adopted ΛCDM parameters set by the *Wilkinson Microwave Anisotropy Probe* 7 results (Larson et al. 2011): $\sigma_8 = 0.801$, $\Omega_m = 0.266$, $\Omega_\Lambda = 0.734$, $n_s = 0.963$ and $h = 0.71$. Throughout this work, we use the term virial mass M_v to refer to the mass within a sphere of radius R_v that corresponds to an over density of 97 relative to the critical density of the Universe (Bryan & Norman 1998). All simulations were initialized at redshift $z = 125$ unless otherwise specified.

[1] As noted in Teyssier, Johnston & Kuhlen (2012), the Via Lactea II halo does indeed have a massive ($M_v = 6.5 \times 10^{11}$ M$_\odot$) companion at a distance comparable to M31. However, this companion halo and field galaxies nearby are not free of contamination from low-mass particles. The contamination reaches 50 per cent by mass, which has potentially important effects on halo properties.

[2] A term we use roughly to correspond to a ∼2 Mpc sphere from the LG barycenter.

[3] Present-day ($z = 0$) halo catalogues and the main branches of the merger trees are available for public download (http://localgroup.ps.uci.edu/elvis), while access to the full merger trees and particle information will be arranged via email contact with the authors.

2.1 Halo selection

We select LG-like pairs from 50 medium-resolution cosmological simulations, each of a cubic volume 70.4 Mpc on a side with particle mass $m_p = 9.7 \times 10^7$ M$_\odot$ and Plummer-equivalent force softening length 1.4 kpc (comoving). From these cosmological volumes, we selected 12 halo pairs for resimulation using the criteria described below. For each of the 24 haloes included in the ELVIS pairs, we also chose an isolated analogue of identical virial mass (M_v) that is separated by at least 2.8 Mpc from all haloes more massive than $M_v/2$. The isolated set serves as a control sample for comparison.

Our approach to selecting LG regions differs from that of the well-known Constrained Local Universe Simulations (CLUES) project (Gottloeber et al. 2010), which relies on the 'constrained realization' technique to match the observed density and velocity fields on a ∼10 Mpc scales around the LG. The advantage to our approach is that it guarantees a good LG analogue in each resimulation. The downside is that the larger scale density field will usually not be identical to that of the LG. The two initialization methods therefore have different, complementary strengths.

In selecting pairs, we targeted haloes with phase-space characteristics similar to the MW/M31 system, with cuts similar to those of Forero-Romero et al. (2011), based on values of the virial mass of each host ($M_{v,1}$ and $M_{v,2}$, where $M_{v,2} \geq M_{v,1}$), the distance between host centres ΔR, the pair approach velocity and local environment:

(i) *mass of each host:* $10^{12} \leq M_v \leq 3 \times 10^{12}$ M$_\odot$ (Tollerud et al. 2012; Boylan-Kolchin et al. 2013; Fardal et al. 2013; Piffl et al. 2013);
(ii) *total mass:* $2 \times 10^{12} \leq M_{v,1} + M_{v,2} \leq 5 \times 10^{12}$ M$_\odot$ (Li & White 2008; van der Marel et al. 2012);
(iii) *separation:* $0.6 \leq \Delta R \leq 1$ Mpc (McConnachie et al. 2005, and references therein);
(iv) *radial velocity:* $V_{rad} \leq 0$ km s^{-1} (van der Marel et al. 2012) and
(v) *isolation:* no haloes with $M_v \geq M_{v,1}$ within 2.8 Mpc of either centre and no haloes with $M_v \geq 7 \times 10^{13}$ M$_\odot$ within 7 Mpc of either centre (Karachentsev et al. 2004; Tikhonov & Klypin 2009).

We identified 146 halo pairs that met these criteria within the 50 simulations we ran (an equivalent volume of 1.76×10^7 Mpc^3) and selected 12 pairs for resimulation. We intentionally chose several pairs that consisted of hosts with massive ($V_{max} > 75$ km s^{-1}) subhaloes in order to ensure that we had a fair number of systems with realistic analogues to the Large Magellanic Cloud (LMC) and M33; had we selected pairs at random, it would have been unlikely to obtain such massive subhaloes (Boylan-Kolchin et al. 2010). We further made an effort to include two pairs that had very low relative tangential velocities <15 km s^{-1} in order to mimic the low relative tangential speed of the MW/M31 pair (van der Marel et al. 2012). For the isolated control sample, we imposed no selection choices other than in matching virial masses and demanding that there are no haloes with $M > M_v/2$ within 2.8 Mpc. Most of the matches in mass are good to within 5 per cent, though some differ by up to 10 per cent. Though we attempted to match their masses at the per cent level in the low-resolution simulations used to identify objects for resimulation, differences of this order are expected when using the zoom-in technique (Oñorbe et al. 2014).

For record-keeping purposes, each LG–analogue pair is named after a famous duo, as summarized in Table 1. The individual haloes that make up the pairs are referenced by the same names in Table 2. The isolated analogues are identified by the same name prefixed by *i* in Table 3. We discuss the information presented in these tables in

Table 1. Properties of the 12 ELVIS pairs together with associated properties of the MW/M31 pair, where appropriate. Detailed information about the individual haloes that make up these pairs is given in Table 2, where they are referred to by the same names used in column 1.

Pair name	ΔR (kpc)	$V_{\rm rad}$ (km s^{-1})	$V_{\rm tan}$ (km s^{-1})	Total mass[a] (10^{12} M$_\odot$)	Mass ratio[b]	$\mathcal{V}_{\rm res}$[c] (Mpc^3)	$N_{\rm haloes}$[d] ($<\mathcal{V}_{\rm res}$)	$N_{\rm p}$ [e] ($<\mathcal{V}_{\rm res}$)	$[V_3, D_\ell, D_{\rm s}]$[f] (km s^{-1}, Mpc, Mpc)
Zeus & Hera	595	−158.4	173.6	3.98	2.05	39.7	3,956	44M	[73, 0.73, 1.3]
Scylla & Charybdis	705	−21.1	132.4	3.97	1.45	38.1	4,381	47M	[105, 0.50, 1.09]
Romulus & Remus	935	−20.4	13.2	3.15	1.53	34.6	2,522	30M	[62, 0.40, 1.33]
Orion & Taurus	829	−69.8	62.9	4.04	2.38	24.7	2,856	36M	[56, 1.06, 1.90]
Kek & Kauket	1040	−32.3	38.6	3.25	2.06	43.2	3,461	40M	[114, 0.96, 1.68]
Hamilton & Burr	941	−18.0	37.7	3.26	1.17	24.7	2,882	32M	[54, 1.39, 0.57]
Lincoln & Douglas	780	−86.6	42.4	3.89	1.90	18.2	2,801	33M	[60, 1.86, 1.16]
Serena & Venus[g]	687	−109.0	71.0	4.26	1.94	24.9	4,797	55M	[159, 0.89, 1.54]
Sonny & Cher	966	−104.9	42.0	3.69	1.05	9.7	2,290	29M	[84, 0.99, 0.84]
Hall & Oates	980	−8.9	43.7	2.71	1.26	14.5	1,713	24M	[64, 1.07, 1.59]
Thelma & Louise	832	−52.4	11.0	2.36	1.30	5.3	1,693	20M	[64, 1.13, 0.46]
Siegfried & Roy[g]	878	−68.5	57.6	4.31	1.02	11.9	5,087	61M	[157, 0.61, 1.09]
Milky Way & M31	770 ± 80[h]	-109 ± 9[h]	<52[h]	3.8 ± 0.7[i]	$1.26\ ^{+0.69}_{-0.24}$[j]	–	–	–	[64, 0.89, 0.45][k]

[a] Sum of virial masses: $M_{\rm v,1} + M_{\rm v,2}$.
[b] Ratio of virial masses: $M_{\rm v,2}/M_{\rm v,1}$, where $M_{\rm v,2} \geq M_{\rm v,1}$ by definition.
[c] Bispherical volume of the high-resolution region at $z = 0$ that is uncontaminated by low-resolution particles. Specifically, $\mathcal{V}_{\rm res}$ is defined as the union of the two maximal spheres, centred on each pair, that are uncontaminated.
[d] Number of identified haloes with $V_{\rm max} > 8\,{\rm km\,s^{-1}}$ that sit within the high-resolution volume $\mathcal{V}_{\rm res}$.
[e] Number of particles in millions (rounded to the nearest million) within the high-resolution volume $\mathcal{V}_{\rm res}$.
[f] The value of $V_{\rm max}$ for and distances to the largest halo within 1.2 Mpc of either host that is not within 300 kpc of either host. The distances listed are relative to the larger and smaller of the two hosts, respectively.
[g] In order to avoid bias, these pairs are indicated with dashed lines in Figs 4, 5, B2 and B3 and have been excluded from Figs 6, 7, 8, 11, 12 and 13 because they have large companions at ∼1 Mpc distances.
[h] As given in van der Marel et al. (2012) with 2σ uncertainties quoted.
[i] In listing this value, we average the timing argument result $M_{\rm v,1} + M_{\rm v,2} = (4.3 \pm 1.1) \times 10^{12}$ M$_\odot$ from van der Marel et al. (2012) and the sum of our fiducial $M_{\rm v}^{\rm MW}$ and $M_{\rm v}^{\rm M31}$ values listed in Table 2. Quoted uncertainties are 2σ.
[j] The quoted average and ratio takes into account that the quantity is defined to be larger than unity. It combines the constraints listed in Table 2 and quotes 90 per cent uncertainties.
[k] We list the most luminous galaxy within 1.2 Mpc of either the MW or M31 according to McConnachie (2012): NGC 6822 with $L_{\rm V} = 1.04 \times 10^8$ L$_\odot$ and $M_* = 8.3 \times 10^7$ M$_\odot$. We let $D_\ell = D_{\rm M31}$ and $D_{\rm s} = D_{\rm MW}$. The $V_{\rm max}$ listed for NCG 6822 is very rough, and is based on assuming the AM prescription described in Section 4.1 and the $V_{\rm max}-M$ relation in Fig. 1. Note that the galaxy IC 1613 is only slightly less luminous than NGC 6822 but is approximately 370 kpc closer to M31 and 300 kpc farther from the MW.

Section 2.3. The first pair listed in Table 1, Zeus & Hera, is singled-out in several figures below as a good analogue to the M31/MW system in terms of observed galaxy counts in the local volume region. The halo Hera is identified with the MW in this pairing.

2.2 Zoom simulations

In creating the zoom-in initial conditions for the ELVIS haloes, we broadly followed the methods outlined in Oñorbe et al. (2014), who give prescriptions for selecting regions that will be free from low-resolution particle contamination in the final run. For the pairs, we identified Lagrangian volumes for all particles within $4\,R_{\rm v}$ of either host in the final time step; for the isolated analogues, we use particles within $5\,R_{\rm v}$ in all but one case (specified below). We relied on the public[4] code MUSIC (Hahn & Abel 2011) to create initial conditions associated with these Lagrangian volumes at high resolution. The mass resolution in the zoom regions of our production runs is $m_{\rm p} = 1.9 \times 10^5$ M$_\odot$, corresponding to an effective resolution of 4096^3 in the box. The Plummer-equivalent force softening, ϵ, in these runs was held constant in comoving units until $z = 9$, at which point it was held fixed at 141 pc (physical) for the remainder of each simulation.

The high-resolution regions are surrounded by stepped levels of progressively lower force resolution and higher mass particles, with the majority of the parent boxes (70.4 Mpc cubes) filled with an effective resolution of 128^3 ($m_{\rm p} = 6.2 \times 10^9$ M$_\odot$) and each successive step increasing the effective resolution by a factor of 2 (decreasing the particle mass by a factor of 8). As in the high-resolution regions, ϵ remains constant in comoving units until $z = 9$, then becomes fixed in physical units. These force softenings, however, are significantly larger than in the high-resolution regions: at $z = 0$ in the main runs, the two highest particle masses utilize $\epsilon = 56$ kpc, the two intermediate regions use $\epsilon = 4.2$ kpc and, $\epsilon = 704$ pc for the particles immediately surrounding the high-resolution volume.

Self-bound dark matter clumps are identified with the six-dimensional halo finder ROCKSTAR (Behroozi, Wechsler & Wu 2013a) and followed through cosmic time with CONSISTENT-TREES (Behroozi et al. 2013b). Both of these codes are publicly available.[5] Subhalo masses (M) are calculated by ROCKSTAR and correspond to the bound mass of the system. Maximum circular velocities ($V_{\rm max}$) correspond to the peak of the circular velocity curve, $V_c(r) = \sqrt{GM(r)/r}$, at a given redshift. We also checked results at the final time step ($z = 0$) against the public,[6]

[4] The link is http://www.phys.ethz.ch/hahn/MUSIC/

[5] The links are http://code.google.com/p/rockstar/ and http://code.google.com/p/consistent-trees/.

[6] The link is http://popia.ft.uam.es/AHF/

Table 2. Properties of the 24 haloes that comprise our LG sample, along with the properties of the MW and M31, where appropriate. The haloes are listed in the same order as in Table 1, and identified by the names in column 1 of that table. All values in this table are relative to the centre of the each host; equivalent properties for the isolated sample are listed in Table 3, where identical names with preceding *i*'s may be used to identified mass-matched analogues. The table is discussed in Section 2.

Halo	$M_{\rm v}$ ($10^{12}\,{\rm M}_\odot$)	$V_{\rm v}$ (km s^{-1})	$V_{\rm max}$ (km s^{-1})	$R_{\rm v}$ (kpc)	c_{-2} [a]	$z_{0.5}$ [b]	$N_{\rm haloes}$ [c] ($<R_{\rm v}$)	$N_{\rm haloes}$ [d] (<300)	Max $V_{\rm max}$ [e] (km s^{-1})	$R_{\rm res}$ [f] (Mpc)	$N_{\rm p}$ [g] ($<R_{\rm res}$)	$N_{\rm haloes}$ [h] ($<R_{\rm res}$)
Hera	1.30	140	159	285	7.9	0.79	397	435	89	1.33	39M	3,348
Zeus	2.67	178	203	362	5.6	1.08	1,029	880	70	1.92	44M	3,955
Scylla	1.62	151	179	306	6.4	1.24	577	567	84	1.28	36M	3,171
Charybdis	2.35	171	208	346	7.6	0.89	896	785	77	1.91	47M	4,368
Romulus	1.90	159	197	323	9.6	1.57	623	579	54	1.76	30M	2,427
Remus	1.24	138	177	280	12.3	1.53	440	463	40	1.42	26M	2,027
Orion	2.84	182	225	369	5.3	1.61	955	775	47	1.60	35M	2,784
Taurus	1.19	136	169	276	10.9	1.08	383	419	61	1.21	31M	2,321
Kek	2.19	167	205	338	13.7	0.64	685	609	43	1.87	39M	3,333
Kauket	1.06	131	157	266	9.6	1.10	388	426	64	1.56	32M	2,687
Hamilton	1.76	155	197	315	9.9	1.47	582	560	62	1.39	28M	2,494
Burr	1.50	147	173	299	10.6	1.18	613	615	39	1.48	29M	2,529
Lincoln	2.55	176	199	356	8.4	1.36	941	780	75	1.27	31M	2,559
Douglas	1.34	142	169	287	9.6	0.99	412	430	89	1.32	31M	2,558
Serena	2.81	181	222	368	14.4	1.77	911	743	61	1.48	51M	4,418
Venus	1.45	145	156	295	1.8	0.98	612	623	83	1.39	45M	3,879
Sonny	1.89	159	180	322	2.4	0.30	664	637	115	0.97	20M	1,480
Cher	1.80	156	171	317	11.0	0.66	580	552	81	1.12	27M	2,082
Hall	1.52	148	180	299	10.3	1.04	437	438	50	1.35	23M	1,560
Oates	1.20	136	167	277	8.4	0.62	317	346	76	1.01	17M	1,085
Thelma	1.34	141	169	287	7.1	1.44	421	438	48	0.91	18M	1,379
Louise	1.03	130	157	263	17.0	1.61	357	407	54	0.80	11M	928
Siegfried	2.17	166	195	337	6.5	0.67	827	734	62	1.09	46M	3,674
Roy	2.14	166	194	336	11.1	1.14	702	628	64	1.15	53M	4,325
Milky Way	$1.6\,^{+0.8}_{-0.6}$ [i]	$150\,^{+22}_{-22}$	–	304^{+45}_{-45}	–	–	–	≥ 27[j]	88[k]	–	–	–
M31	1.8 ± 0.65[l]	$156\,^{+17}_{-22}$	–	317^{+35}_{-44}	–	–	–	≥ 32[j]	130[m]	–	–	–

[a] Halo concentration defined as $c_{-2} \equiv R_{\rm v}/r_{-2}$, where r_{-2} is the radius where ρr^2 peaks. This parameter is equivalent to the NFW concentration for haloes that follow perfect NFW profiles (Navarro et al. 1996).
[b] Formation time proxy defined as the redshift z when the main progenitor mass first equalled $0.5\,M_{\rm v}(z=0)$.
[c] Number of subhaloes within $R_{\rm v}$ with $V_{\rm max} > 8\,{\rm km\,s^{-1}}$.
[d] Number of subhaloes within 300 kpc with $V_{\rm max} > 8\,{\rm km\,s^{-1}}$.
[e] $V_{\rm max}$ value of the largest identified subhalo within 300 kpc.
[f] The high-resolution radius, defining a sphere centred on the halo within which there is zero contamination from low-resolution particles.
[g] Number of particles in millions (rounded to the nearest million) within the high-resolution radius $R_{\rm res}$.
[h] Number of subhaloes within $R_{\rm res}$ with $V_{\rm max} > 8\,{\rm km\,s^{-1}}$.
[i] Taken from Boylan-Kolchin et al. (2013) with 90 per cent c.l. quoted.
[j] As enumerated in McConnachie (2012).
[k] The LMC from Olsen et al. (2011)
[l] Combining results from Fardal et al. (2013) and van der Marel et al. (2012) who obtain $M_{\rm v}^{M31} = (2.1 \pm 1.0) \times 10^{12}$ and $(1.5 \pm 0.8) \times 10^{12}$, respectively, with 2σ errors quoted.
[m] The Triangulum galaxy (M33), from Corbelli (2003).

spherical overdensity-based AMIGA HALO FINDER (Knollmann & Knebe 2009) and found that the results did not differ significantly and were identical within the statistical variation of our sample of haloes.[7]

Three of the most useful quantities that can be determined for haloes in our simulations are $M_{\rm peak}$ (the maximum mass of a dark matter structure over its history), $a_{\rm peak}$ (the latest scale factor at which $M_{\rm peak}$ occurs) and $V_{\rm peak}$ (the maximum circular velocity at $a_{\rm peak}$). To define these quantities, one must adopt an unambiguous definition of the main branch of each halo's merger tree. We assign the main progenitor at each time step as the branch of the tree with the most total mass up to and including that time step, i.e. the sum of $M_{\rm v}$ for all haloes over all preceding time steps in that branch. This definition weights both the formation time and the virial mass of haloes in a given branch. The final step in our pipeline identifies the main branch of each merger tree and extracts $M_{\rm peak}$, $V_{\rm peak}$ and $a_{\rm peak}$ for each halo with $z = 0$ quantities M (or $M_{\rm v}$ for hosts) and $V_{\rm max}$.

We simulated three of the isolated analogues (iScylla, iKauket, and iHall) at higher resolution, with $m_{\rm p} = 2.35 \times 10^4\,{\rm M}_\odot$ (8192^3 effective particle number) and $\epsilon = 70.4$ pc; we refer to these runs as the HiRes simulations. The HiRes version of iKauket was originally simulated in the context of previous work (Oñorbe et al. 2014) and was initialized at a different redshift ($z = 250$) than the rest of our runs. It also used a Lagrangian volume chosen from all

[7] Though our results presented here and made publicly available upon publication rely on ROCKSTAR, we are happy to supply associated AMIGA HALO FINDER catalogues upon request.

Table 3. Properties of the 24 isolated haloes that are mass matched to the haloes in our LG analogues. The name identifies the paired halo with a nearly identical mass, the properties of which are listed in Table 2, and the preceding *i* indicates an isolated analogue. Columns are identical to those in Table 2. The last three rows correspond to the HiRes simulations of three haloes.

Halo	M_v (10^{12} M$_\odot$)	V_v (km s^{-1})	V_{max} (km s^{-1})	R_v (kpc)	c_{-2} [a]	$z_{0.5}$ [b]	N_{haloes} [c] ($<R_v$)	N_{haloes} [d] ($<$300)	Max V_{max} [e] (km s^{-1})	R_{res} [f] (Mpc)	N_p [g] ($<R_{res}$)	N_{haloes} [h] ($<R_{res}$)
iHera	1.22	137	163	278	7.9	0.8	420	450	41	1.54	17M	1,348
iZeus	2.59	176	205	358	5.5	1.3	925	773	60	1.76	27M	2,312
iScylla	1.59	150	176	304	9.9	0.97	437	436	84	1.56	20M	1,500
iCharybdis	2.29	169	207	343	13.7	1.4	758	643	51	1.72	25M	2,125
iRomulus	1.97	161	186	327	11.3	0.88	792	734	75	1.89	21M	1,899
iRemus	1.31	141	166	285	8.0	0.91	494	515	54	1.40	14M	1,261
iOrion	2.84	182	218	369	4.9	1.64	1,179	1,015	54	2.06	37M	3,315
iTaurus	1.23	138	165	279	10.4	1.36	453	481	46	1.75	14M	1,315
iKek	2.41	172	204	349	5.5	0.74	705	618	71	1.63	27M	2,267
iKauket†	1.02	129	157	262	11.1	0.97	278	327	39	2.12	21M	1,730
iHamilton	1.86	158	203	321	14.2	2.11	566	523	57	1.55	17M	1,309
iBurr	1.56	149	179	302	13.6	0.75	548	540	66	1.61	15M	1,279
iLincoln	2.62	177	213	359	13.8	0.89	813	702	83	1.35	27M	2,017
iDouglas	1.30	140	180	285	16.1	1.76	375	383	49	1.93	15M	1,107
iSerena	2.67	178	212	361	11.4	1.15	952	817	81	1.66	26M	2,218
iVenus	1.39	143	179	291	14.3	1.41	461	483	46	2.15	32M	2,684
iSonny	1.68	153	187	310	4.5	0.69	647	632	117	2.01	20M	1,877
iCher	1.92	160	170	324	6.4	0.6	701	660	63	2.23	22M	1,888
iHall$^\diamond$	1.71	148	172	300	6.0	1.13	528	528	92	1.59	16M	1,264
iOates	1.20	136	157	277	8.4	0.72	444	478	78	1.58	13M	1,068
iThelma	1.39	143	188	291	9.6	1.56	407	421	37	1.95	14M	1,043
iLouise	1.01	129	155	261	8.4	1.22	378	414	49	2.41	14M	1,253
iSiegfried	2.40	172	211	349	11.1	1.42	733	643	55	1.36	21M	1,589
iRoy	2.26	169	205	342	3.9	1.11	844	769	103	1.75	22M	1,850
iScilla HiRes	1.61	150	175	305	9.5	0.95	419 (3,824)*	413 (3,770)*	87	1.54	155M	1,491 (12,509)*
iKauket HiRes‡	1.03	130	158	263	11.8	1.0	277 (2,279)*	324 (2,620)*	38	0.4	56M	446 (3,493)*
iHall HiRes	1.67	152	167	309	5.8	1.07	608 (5,266)*	592 (5,114)*	93	1.59	125M	1,286 (11,176)*

[a]Halo concentration defined as $c_{-2} \equiv R_v/r_{-2}$, where r_{-2} is the radius where ρr^2 peaks. This parameter is equivalent to the NFW concentration for haloes that follow perfect NFW profiles (Navarro et al. 1996).
[b]Formation time proxy defined as the redshift z when the main progenitor mass first equalled $0.5\,M_v(z=0)$.
[c]Number of subhaloes within R_v with $V_{max} > 8$ km s^{-1}.
[d]Number of subhaloes within 300 kpc with $V_{max} > 8$ km s^{-1}.
[e]V_{max} value of the largest identified subhalo within 300 kpc.
[f]The high-resolution radius, defining a sphere centred on the halo within which there is zero contamination from low-resolution particles.
[g]Number of particles in millions (rounded to the nearest million) within the high-resolution radius R_{res}.
[h]Number of subhaloes within R_{res} with $V_{max} > 8$ km s^{-1}.
†iKauket was initialized at $z = 250$ for both the fiducial and HiRes runs.
$^\diamond$Differences in the phase of subhalo orbits between this run and the HiRes equivalent result in the largest subhalo ($V_{max} = 93$ km s^{-1}) being located just beyond R_v at the fiducial resolution. To show convergence with the HiRes run, we include the mass of that halo in the virial mass of iHall and list it in column 10, though it is just beyond 300 kpc. The uncorrected substructure counts are also divergent, but the number of objects within 400 kpc agrees within 5 per cent. The uncorrected mass (1.53×10^{12} M$_\odot$) also agrees with the paired halo, Hall, to within 1 per cent.
*Values in parentheses correspond to subhalo counts down to $V_{max} > 4$ km s^{-1}, the estimated completeness limit of the HiRes simulations.
‡This halo was initialized with a smaller Lagrange volume of high-resolution particles than the rest, which is why it has an anomalously small high-resolution radius.

particles within $2\,R_v$ (rather than our fiducial $5\,R_v$ for the other isolated systems). The standard resolution version of iKauket also started at $z = 250$. As Oñorbe et al. (2014) showed, any variation in halo properties at low redshifts introduced by such a change in initial redshift are comparable to expected variations upon resimulation due to numerical 'minichaos' (Miller 1964), which should be unimportant for our purposes.

Our HiRes simulations are comparable in mass and force resolution to the Aquarius level 2 simulations (Springel et al. 2008) and to Via Lactea I (Diemand, Kuhlen & Madau 2007a), though two of them (iScylla and iHall) have uncontaminated high-resolution volumes – uncontaminated spheres of radius ∼1.5 Mpc around each host – that extend much farther from the halo centres than any previous runs of this kind. The HiRes simulations will facilitate several inquiries that are not possible with our fiducial runs, but for the purposes of this paper, they have allowed us to self-consistently identify the completeness limit for subhaloes in our main ELVIS suite. We find that we are complete to $M > 2 \times 10^7$ M$_\odot$, $V_{max} > 8$ km s^{-1},

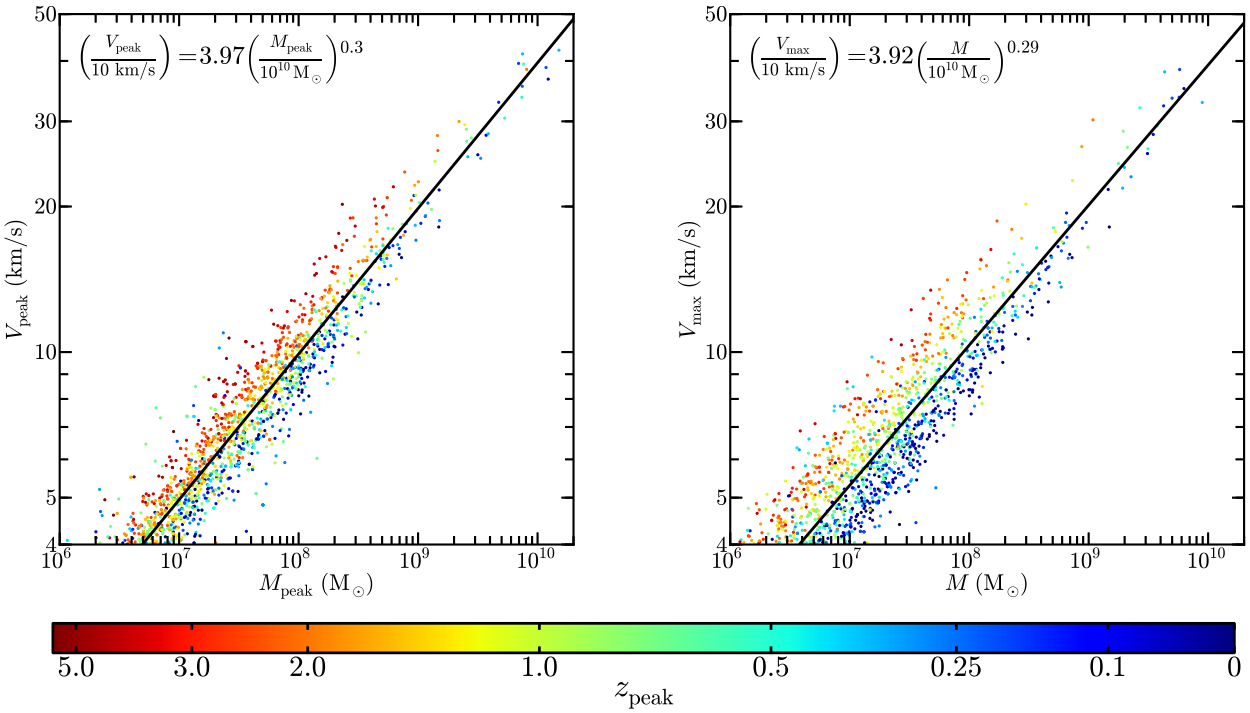

Figure 1. The relation between peak circular velocity and mass at $a_{\rm peak}$ (left) and at $z = 0$ (right) The indicated fit includes all resolved haloes within 400 kpc of iKauket in the HiRes run (though the results do not differ at the fiducial resolution). Each subhalo is coloured by the redshift at which it reached its peak mass ($a_{\rm peak}$); this quantity is well correlated with the scatter about the fits and, as is evident from the right-hand panel, the amount of tidal stripping each subhalo has undergone.

$M_{\rm peak} > 6 \times 10^7\,{\rm M}_\odot$ and $V_{\rm peak} > 12\,{\rm km\,s^{-1}}$. The numerical convergence of our results in $V_{\rm max}$ and $M_{\rm peak}$ is demonstrated explicitly for iKauket in Appendix A.

In the bulk of this paper, we will enumerate haloes and subhaloes based on $M_{\rm peak}$. One could equivalently present results in terms of M, $V_{\rm max}$ or $V_{\rm peak}$ ($V_{\rm max}$ functions are presented Appendix B). Fig. 1 demonstrates the relationship between $M_{\rm peak}$ and $V_{\rm peak}$ (left-hand panel) and M and $V_{\rm max}$ (right-hand panel) for haloes within 400 kpc of the HiRes version of iKauket (the results are indistinguishable for the fiducial resolution runs for $V_{\rm max} > 8\,{\rm km\,s^{-1}}$ and $M_{\rm peak} > 6 \times 10^7\,{\rm M}_\odot$). The best-fitting $M_{\rm peak}-V_{\rm peak}$ and $M-V_{\rm max}$ relations are given by the formulas in the figures themselves.

What is the origin of the scatter in the $V-M$ relations? The points in Fig. 1 are coloured by $z_{\rm peak} = a_{\rm peak}^{-1} - 1$. We see that this variable is strongly correlated with the scatter in V at fixed M, such that earlier forming haloes have higher values of $V_{\rm peak}$ and $V_{\rm max}$. The correlation between $a_{\rm peak}$ and $V_{\rm peak}$ is related to the redshift dependence of the virial overdensity. At early times, haloes at fixed mass have a higher $V_{\rm max}$. The red points effectively sample a population of haloes at $z > 3$, whereas the blue points correspond to haloes in the field at $z \lesssim 0.1$. The correlation between $a_{\rm peak}$ and $V_{\rm max}$ is a combination of the $a_{\rm peak}-V_{\rm peak}$ correlation and the effects of orbital evolution on subhalo density structure (for discussions on these expected trends see, e.g. Zentner & Bullock 2003; Kazantzidis et al. 2004; Diemand, Kuhlen & Madau 2007b).

2.3 General properties of the ELVIS haloes

Table 1 summarizes the names and some properties of the ELVIS pairs at $z = 0$ (along with comparative information for the MW and M31, where appropriate). We include the physical separation between halo centres, their relative radial and tangential velocities,[8] as well as their virial masses and virial mass ratios. Column 7 lists a conservative estimate of the high-resolution simulation volume $\mathcal{V}_{\rm res}$, defined as the union of the two maximal spheres, centred on each pair, that is uncontaminated by any lower resolution particles. Columns 8 and 9 list the overall number of haloes (above our completeness limit of $V_{\rm max} > 8\,{\rm km\,s^{-1}}$) and number of simulation particles contained within the volume $\mathcal{V}_{\rm res}$. The final column lists the $V_{\rm max}$ value of and distances to the largest halo within 1.2 Mpc of either host (but outside of the 300 kpc virial region), which serve as an indication of the larger scale environment. Note that the virial volumes of Hera and Zeus slightly overlap; however, only a single subhalo is identified in that overlapping volume, so the effect on subsequent results is negligible.

Two of the pairs – Siegfried & Roy and Serena & Venus – have a particularly large halo ($V_{\rm max} = 157, 159\,{\rm km\,s^{-1}}$) within 1.2 Mpc of one of the hosts. This may seem contrary to our isolation criteria, but in both cases this third halo is less massive than either of the paired hosts. Nevertheless, the presence of the massive companions may render these pairs less than ideal comparison sets for the real LG. In all figures below that make predictions for the overall count of galaxies expected within $\sim$ Mpc scales, we either remove these two pairs entirely, or show the affected systems with dashed lines.

Fig. 2 shows visualizations of our LG analogues coloured by the locally smoothed density; each box renders a cube 1.5 Mpc on a side centred on the mid-point of the two hosts. Pair names are indicated and the visualizations are rotated such that the pair is aligned with

[8] The kinematics of our pairs as listed in Table 1 are consistent with those found for a larger number of pairs in simulations by Forero-Romero et al. (2013).

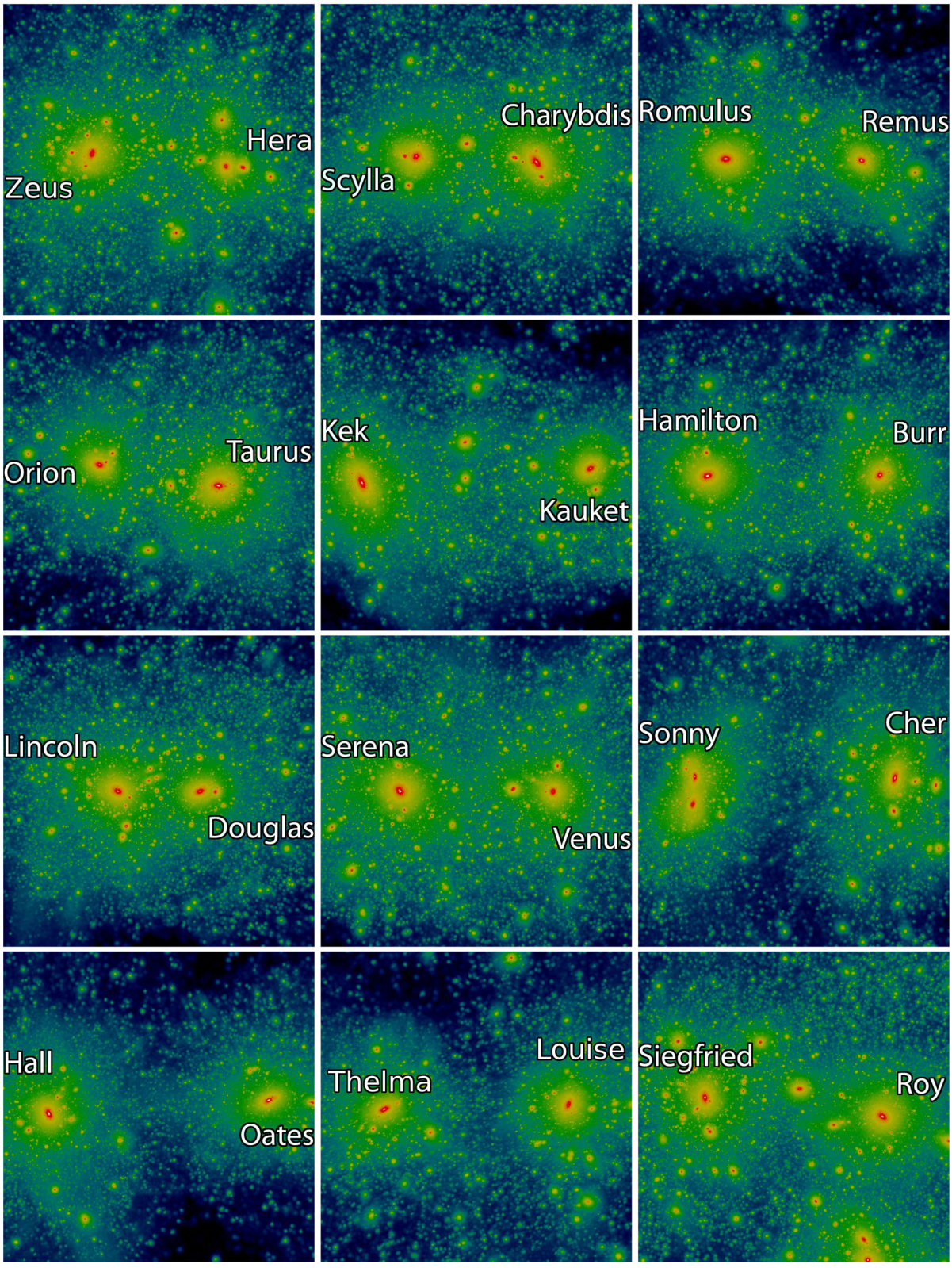

Figure 2. Visualizations of the ELVIS pairs, shown in cubes 1.5 Mpc on a side, each centred on the mean centre of the pair with names given.

the horizontal axis, though not necessarily with an orientation that maximizes the apparent separation. Each of these images is fully resolved without contamination from low-resolution particles, so the shape of the density fields represented are accurate. There are a number of features of interest in these images. For example, it is readily apparent that Sonny (of Sonny & Cher in the bottom row) is undergoing a major merger. It has a subhalo of $V_{\rm max} = 115\,{\rm km\,s^{-1}}$, which is comparable to the host halo's $V_{\rm max} = 180\,{\rm km\,s^{-1}}$ – not

unlike M33 paired with M31. Also, the third massive object near Siegfried & Roy (as discussed above) is evident in the bottom-right panel. As we will discuss below, Zeus & Hera (upper left) furnishes a particularly good match to the LG in many observational comparisons – the 89 km s^{-1} subhalo of Hera is shown on the right.

We list the properties of the individual haloes that comprise each pair in Table 2 along with comparative information for the MW and M31, when appropriate. A similar list for the isolated mass-matched analogues is given in Table 3. In each table, columns 2 through 5 list $M_{\rm v}$, $V_{\rm v}$, $V_{\rm max}$ and $R_{\rm v}$, respectively. Column 6 gives a measure of the halo concentration, $c_{-2} \equiv R_{\rm v}/r_{-2}$, where r_{-2} is the radius where ρr^2 peaks [equivalent to the concentration parameter for haloes that follow Navarro, Frenk & White (1996, NFW) profiles]. Column 7 provides a measure of the halo formation redshift, $z_{0.5}$, defined when the main progenitor first obtains half its current mass. Columns 8 and 9 list the number of $V_{\rm max} > 8\,{\rm km\,s^{-1}}$ subhaloes within $R_{\rm v}$ and 300 kpc, respectively, and column 10 lists the $V_{\rm max}$ of the largest subhalo within 300 kpc. Column 11 gives $R_{\rm res}$, the radius of the largest sphere within which there are no low-resolution particles (an indication of the high-resolution volume size). Columns 12 and 13 list the number of particles (in millions, rounded to the nearest million) and number of identified haloes (with $V_{\rm max} > 8\,{\rm km\,s^{-1}}$) within $R_{\rm res}$ for each halo.

Note that in what follows we will occasionally present results for a region we define as the local volume – the union of two spheres of radius 1.2 Mpc centred on each host. As can be seen from column 11 of Table 2, four of our pairs are technically contaminated in this region (Sonny & Cher, Hall & Oats, Thelma & Louise and Siegfried & Roy). However, the mass fraction of low-resolution particles in the effected volumes is minimal (0.01, 0.007, 0.06 and 0.0008 per cent, respectively) so the practical effects on our results should be negligible (see, e.g. Oñorbe et al. 2014).

Before devoting the next section to a detailed comparison of paired versus unpaired hosts, we mention that we find no statistical difference in the c_{-2} and $z_{0.5}$ distributions between the two sets. Though two of our haloes (Serena and Sonny) that happen to be members of pairs have anomalously low c_{-2} values, we suspect that in Sonny's case this is a result of an ongoing major merger. The median formation redshifts for our paired and unpaired samples are both $z_{0.5} \simeq 1.1$, with no indication that paired halo formation times correlate.

The lack of difference in the $z_{0.5}$ distribution between the two samples is consistent with the comparison made by Forero-Romero et al. (2011) using similarly paired haloes found in the Bolshoi simulations. These authors point out that the three LG-like pairs identified in the constrained CLUES simulations have anomalously early formation times, all three with half-mass formation times $z_{0.5} \gtrsim 1.5$. Three of our 12 paired systems are similarly early forming (Romulus & Remus, each with $z_{0.5} \simeq 1.6$), Orion & Taurus (with $z_{0.5} = 1.6$ and 1.3, respectively), and Thelma & Louise (with $z_{0.5} = 1.4$ and 1.6).

3 PAIRED VERSUS ISOLATED GALAXIES

3.1 Halo abundances

We begin by examining the abundance of dark matter structures, characterized by their $M_{\rm peak}$ values, within various radial boundaries; counts as a function of $V_{\rm max}$ are presented in Appendix .

Fig. 3 shows the cumulative $M_{\rm peak}$ functions for subhaloes within $R_{\rm v}$, normalized to the host halo virial mass $M_{\rm v}$, for each of the 48 hosts in ELVIS. Isolated hosts are shown as thin magenta lines and

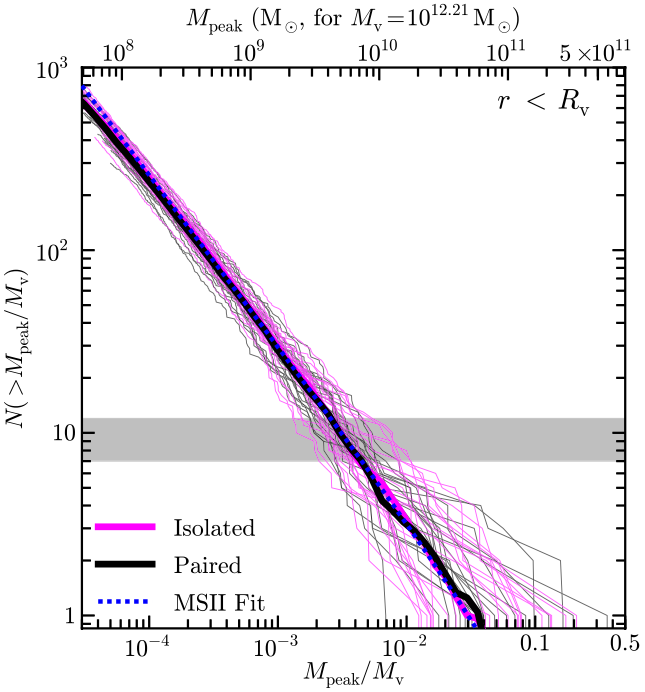

Figure 3. Cumulative subhalo peak mass function ($M_{\rm peak}$) normalized by host $M_{\rm v}$ for each isolated (thin magenta lines) and paired (thin black lines) host. All objects within $R_{\rm v}$ are plotted. The average for each population is shown by the thick lines of corresponding colour. Statistically, the mass functions for paired and isolated hosts are indistinguishable, though the halo-to-halo scatter is large. The upper axis is scaled to the subhalo $M_{\rm peak}$ values assuming a host virial mass of $M_{\rm v} = 1.6 \times 10^{12}\,{\rm M}_\odot$, which is our fiducial MW mass. Thin lines are truncated at $M_{\rm peak} = 6 \times 10^7\,{\rm M}_\odot$, the completeness limit of our simulation catalogues. The grey band shows the range in number of satellites around the MW and M31 with stellar masses above $10^6\,{\rm M}_\odot$; from this band, one can see that such galaxies would be expected to form in haloes more massive than $M_{\rm peak} \simeq 3 \times 10^{-3} M_{\rm v} \simeq 5 \times 10^9\,{\rm M}_\odot$.

the paired hosts are plotted in black. The two distributions clearly overlap. The thick lines denote the mean cumulative count at fixed $M_{\rm peak}/M_{\rm v}$ for the isolated (magenta) and paired (black) populations. Both distributions are well fitted at the low-mass end by a power law:

$$N_{\rm v}(>M_{\rm peak}) = 3.85 \left(\frac{M_{\rm peak}}{0.01\,M_{\rm v}}\right)^{-0.9}. \quad (1)$$

Within $R_{\rm v}$, subhalo counts within isolated and paired haloes in ELVIS are indistinguishable. Even for high-mass subhaloes, where the intrinsic scatter in the counts is large, the means agree well. The blue dashed line, which sits practically on top of the ELVIS means, shows the mean power-law fit obtained by Boylan-Kolchin et al. (2010) for subhaloes in a large sample of MW-mass haloes from the Millennium-II Simulation (MS-II; Boylan-Kolchin et al. 2009). The same fit also matches the substructure counts from the Aquarius simulations (Springel et al. 2008) well. The agreement between our simulations and MS-II/Aquarius is remarkable, especially given that the cosmology of these older simulations is slightly different from our adopted values, which are based on more recent constraints.

Broadly speaking, the scatter in subhalo counts among haloes also agrees between the two samples. At small masses ($M_{\rm peak}/M_{\rm v} \lesssim 10^{-3}$) we find that the standard deviation divided by the mean approaches $\sigma/\langle N\rangle \simeq 0.15$, and that the scatter increases towards

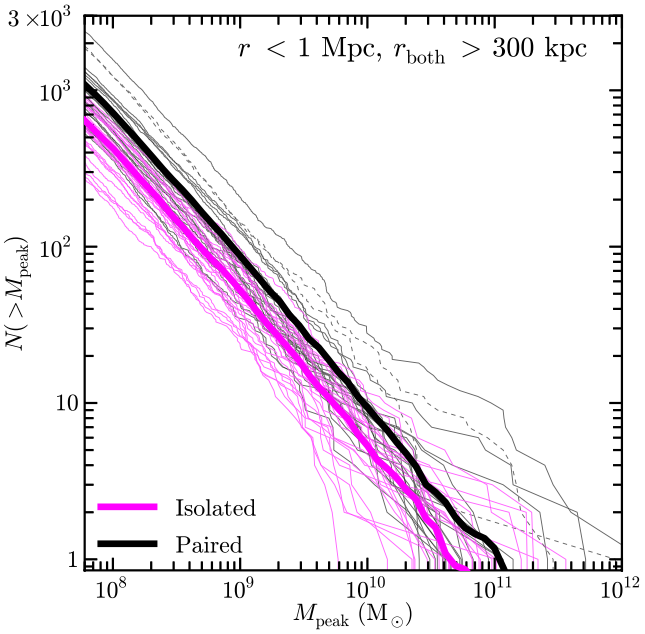

Figure 4. Cumulative counts, as a function of $M_{\rm peak}$, for haloes that are between 300 kpc and 1 Mpc of any host. The paired population (black) has an amplitude that is approximately 80 per cent larger at fixed $M_{\rm peak}$ than that of the isolated analogues (magenta). The environment around a LG pair thus differs noticeably from that of an isolated MW-size halo, even though such differences are not manifest within the virial radius (Fig. 3).

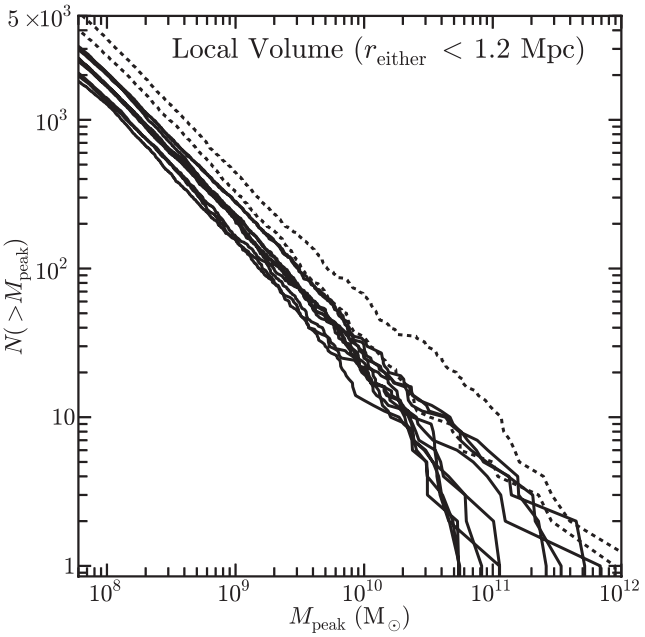

Figure 5. The $M_{\rm peak}$ functions around the LG pairs; each line represents a pair of giants and includes all haloes (excluding the MW and M31 analogues) within 1.2 Mpc of either host, which we define as the local volume. Two pairs contain a third large system within the volume and are thus shown as dashed lines. We predict ∼2000–3000 objects with $M_{\rm peak} > 6 \times 10^7$ M$_\odot$ within the region.

higher masses, with $\sigma/\langle N\rangle \simeq 0.4$ at $M_{\rm peak} \simeq 0.01 M_{\rm v}$. This result is consistent with an intrinsic halo-to-halo scatter of ∼15 per cent in the abundance of substructure reported elsewhere (Boylan-Kolchin et al. 2010; Busha et al. 2011; Wu et al. 2013).

Though we do not plot it, the $z = 0$ (bound) mass functions also agree well within $R_{\rm v}$ and are both well fitted by

$$N_{\rm v}(>M) = 1.11 \left(\frac{M}{0.01\,M_{\rm v}}\right)^{-0.95}, \quad (2)$$

though the scatter is slightly larger than in the $M_{\rm peak}$ function ($\sigma/\langle N\rangle \sim 0.2$ at small masses).

One take away from this initial result is that predictions for subhalo counts within the virial radius from previous high-resolution simulations that studied isolated MW-size hosts (e.g. Diemand et al. 2008; Kuhlen et al. 2008; Springel et al. 2008) are not expected to be significantly different than those for paired haloes like the MW and M31.

At distances beyond the virial radii of either host, the presence of a massive companion should affect halo abundances. To compare the counts at large distances between isolated and paired MW-size haloes, we must avoid the bias that would be introduced by simply counting all haloes at a given distance, as many will be subhaloes of the M31 analogue in the paired systems. We attempt to remove this bias by defining a region around each host that we call the 'local field': a spherical shell between 300 kpc and 1 Mpc of the centre of that host, but excluding the region within 300 kpc of the centre of the other giant. That is, no subhaloes of either LG giant analogue are included in this region.

We plot the $M_{\rm peak}$ function for these local field regions around all the ELVIS haloes in Fig. 4. The environment surrounding a typical LG-like halo is richer than that around an isolated system, even when the partner's subhaloes are removed. Specifically, the average relations are again well fitted at the low-mass end by power laws, but the normalization for the paired sample is about 80 per cent higher than that of the isolated sample:

$$N_{0.3-1}(>M_{\rm peak}) = N_0 \left(\frac{M_{\rm peak}}{10^{10}\,{\rm M}_\odot}\right)^{-0.9}, \quad (3)$$

with $N_0 = 6.4$ for the isolated sample and $N_0 = 11$ for the paired sample. The dashed lines in Fig. 4 indicate the two haloes that have a large companion within the 0.3−1 Mpc region (see Section 2.3 and Table 1). It is possible that these systems are poor comparison sets to the LG, which appears to lack such a galaxy (Table 1). If we remove the dashed lines from the fit, the normalization for the paired systems becomes $N_0 = 9.2$, which is ∼56 per cent higher than that for the isolated sample (removing the isolated counterparts to those haloes also gives a slightly lower normalization $N_0 = 5.9$). While the distributions show some overlap, the presence of a paired companion appears to bias the overall large-scale environment to be substantially richer in small haloes, even when the subhaloes of the paired host are excluded from the counts.

Fig. 5 presents total halo number counts as a function of $M_{\rm peak}$ within a bispherical volume defined by overlapping spheres of radius 1.2 Mpc of each paired host. There is one line for every ELVIS pair, thus each can be regarded as a realization of the LG itself. The dashed lines indicate the two pairs that have large companions in the region, possibly making them less than ideal comparison sets for the LG. Neglecting those two systems, the group-to-group scatter in this local volume mass function is remarkably tight, spanning less than a factor of ∼2 over all 10 realizations for masses $M_{\rm peak} \lesssim 10^{10}$, M$_\odot$. In total, the best LG analogues in the ELVIS suite have 2000−3000 haloes with $M_{\rm peak} > 6 \times 10^7$ M$_\odot$ in this local volume region. Of course, many of these small haloes likely contain galaxies that are either devoid of stars entirely, or too faint to detect with current methods. We investigate implications for the number of observable galaxies throughout this region in Section 4.

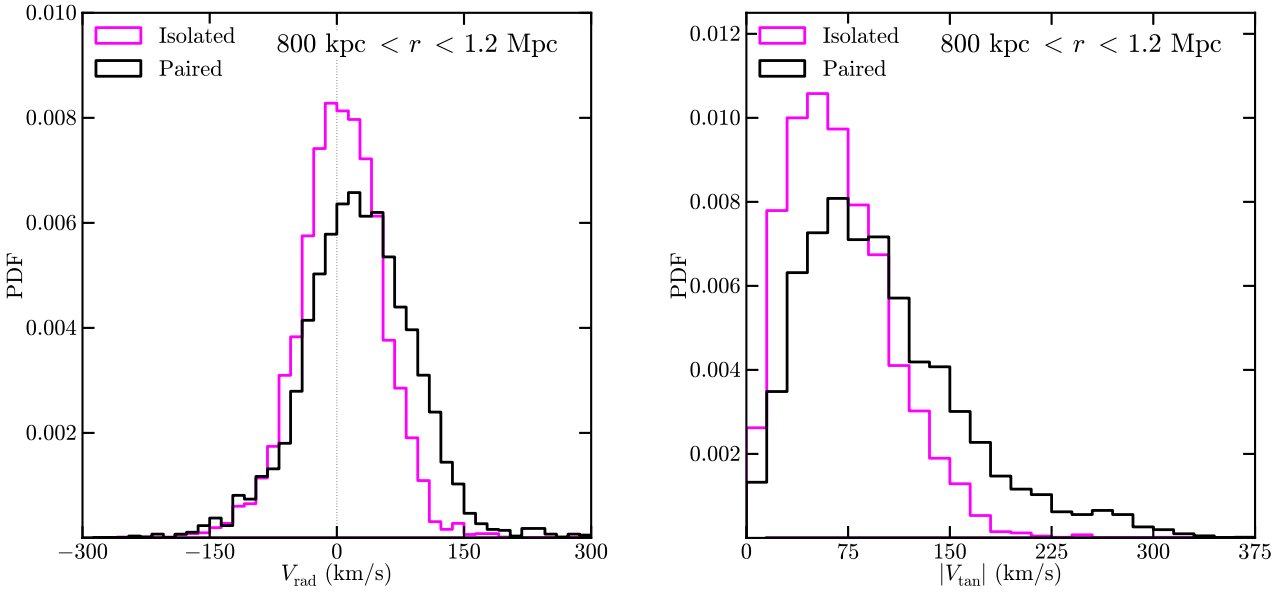

Figure 6. Stacked distributions of radial (left-hand panel) and tangential (right-hand panel) velocities for haloes around the isolated (magenta) and paired (black) haloes at distance of 0.8−1.2 Mpc from the *nearest* host. While the distributions for paired and isolated haloes are the same within $R_{\rm v}$ (not plotted), the differences become pronounced at large radii, with paired environments being substantially hotter. While essentially all haloes ∼1 Mpc from isolated MW analogues have $V_{\rm tan} < 200\,{\rm km\,s^{-1}}$, a large fraction around LG analogues have $V_{\rm tan} > 200\,{\rm km\,s^{-1}}$. It is also apparent that while the radial velocities of haloes at ∼1 Mpc distance from isolated MW-like hosts are centred on zero, the paired analogues have an excess population of outflowing systems. These outflowing systems include a 'backslash' population that is larger among pairs (see Section 3.3) and also objects that have yet to turn around from the Hubble flow (the zero velocity surface is centred on the pair at ∼1 Mpc distance, not the individual host). One broad implication of this figure is that in order to correctly predict the large-scale velocity field around the MW, one must account for the presence of M31.

3.2 Halo dynamics

We expect that the presence of M31 alters the dynamical structure of the MW's local environment relative to the environment of an isolated analogue. While we find that, within ∼300 kpc of the hosts, the paired and isolated samples have indistinguishable subhalo kinematics, regions beyond this distance show distinct kinematical differences.

Fig. 6 shows stacked distributions of radial and tangential velocities for $M_{\rm peak} > 6 \times 10^7\,{\rm M}_\odot$ haloes having distances between 800 kpc and 1.2 Mpc of a giant. Note that in these histograms, we compute the distance to both of the hosts and only use the smaller of the two distances (i.e. all haloes at distance r from one host are at least that same distance r from the other host). Regions surrounding isolated hosts are shown in magenta while regions around paired systems are in black. The kinematic distinction is clear: paired haloes are both kinematically hotter and show an excess of systems that are outflowing at this radius. As we discuss in the next subsection, this enhanced population of outflowing haloes includes a large number of objects that were once within the virial radius of one of the giants. This fraction appears to be higher in paired hosts. A complication when interpreting the radial velocity figure is that the zero-velocity/turn-around surface (at ∼1 Mpc distance) for the pairs is centred between the hosts rather than on the main halo as it is for the isolated analogues. This means that some fraction of the haloes in this diagram may not have turned around from the Hubble flow.

In the histograms shown in Fig. 6, we have removed haloes belonging to the pairs Siegfried & Roy and Serena & Venus. As discussed above, these pairs have a particularly large halo within 1.2 Mpc of one of the hosts, and therefore may be poor analogues to the real LG. Including them only serves to make the overall paired histograms even hotter compared to the isolated analogues.

3.3 Backsplash haloes

Here we investigate the dynamical histories of each small halo in the vicinity of our MW analogues at $z = 0$, and specifically ask whether a halo has been within the virial radius of either giant since $z = 5$. If so, then in principle, environmental effects such as ram pressure, harassment or strangulation could have quenched the galaxy and it hosts (Boselli et al. 2008; Kawata & Mulchaey 2008; Grcevich & Putman 2009; Woo et al. 2013; Phillips et al. 2014). We refer to previously interacted objects of this kind as 'backsplash' haloes (e.g., Gill, Knebe & Gibson 2005, and references therein). Knebe et al. (2011) identified an additional population of haloes, which they termed 'renegade', that have been a member of both the M31 and MW halo analogues. We reserve a more detailed study of these interesting objects for a future work – for this paper, we combine renegade haloes beyond $R_{\rm v}$ with all other backsplash haloes and those within $R_{\rm v}$ with all other subhaloes.

Fig. 7 presents the differential fraction of haloes that are backsplash objects as a function of distance from each host in radial bins of width $R_{\rm v}/2$. Systems around our LG analogues are shown in black, where the distance assigned is the minimum of the distances to the two giants in the group. As in Fig. 6, we have removed haloes belonging to the two pairs in our sample with large companions at ∼1 Mpc distance. The subsample of haloes that meet the radial cut from the centre of both giants simultaneously are shown in cyan. The isolated sample is shown in magenta. We indicate with open symbols bins where the full halo sample was not used, either due to contamination at large radii or because there are no haloes that meet the radial cut in the bin. The points correspond to the average over all hosts and the error bars denote the full width of the distribution, measured system by system.

Unsurprisingly, the backsplash fraction is largest at small radii. In the regions spanning $1-1.5R_{\rm v}$, typically 70 per cent of haloes

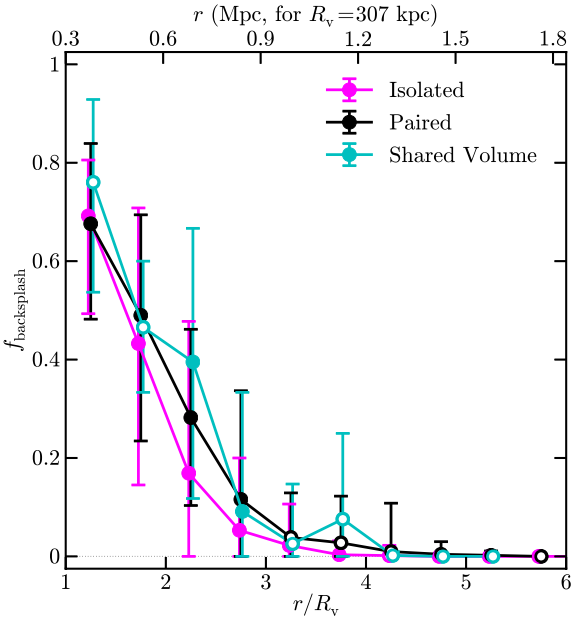

Figure 7. The fraction of $M_{peak} > 6 \times 10^7$ $M_\odot$ haloes at $z = 0$ that have been within R_v of a MW size host as a function of r/R_v from the centre of each host. The points show the average in each radial bin and the error bars denote the full width of the distribution over all hosts. The magenta line corresponds to the isolated sample, and the black line corresponds to paired hosts, where the distance is to the nearest of the two giants. The cyan line also counts systems in the paired simulations, but counts only those systems that simultaneously meet the radial cut for both hosts. The most likely location for backsplash haloes is in this shared volume and between 1 and 2 R_v of both hosts (i.e. in between the two haloes rather than on one side or the other of the LG pair).

have been within R_v since $z = 5$, though that number can be as high as 80 per cent in some cases (also see Mamon et al. 2004; Gill et al. 2005). The interaction fraction in the environment of LG-like pairs is systematically higher than in isolated analogues at large radii, and the overlapping volume (cyan) is particularly rich in objects that have interacted. Indeed, the shared region in the real LG may be the best hunting ground for potential backsplash candidate dwarfs. Remarkably, in our LG-analogue systems, the probability that a halo has interacted only drops to zero at approximately 5 R_v ($\sim$ 1.5 Mpc). Expressed cumulatively (rather than differentially), we find that the overall fraction of backsplash haloes within the 1.2 Mpc local volume regions of our paired hosts ranges from 30 to 52 per cent.

How might backsplash haloes be distinguished observationally throughout the LG? In Fig. 8, we compare the relative tangential and radial velocities of backsplash haloes (grey line) in the $r = 400$–800 kpc radial bins to those that have never accreted (black line). Here we limit ourselves to paired hosts. As in Teyssier et al. (2012), we find that backsplash haloes tend to be outflowing from the host that they have interacted with, whereas those that have not yet accreted are preferentially inflowing. As the right-hand plot shows, we also expect backsplash haloes to have low tangential velocities compared to those that have never been within R_v. The implication is that backslash systems are more likely to be on radial orbits and to be on their way out. At the same time, there is significant overlap in the distributions and it is difficult to disentangle the populations on these specific kinematic properties alone. We reserve a more thorough analysis of this question for a future paper.

4 EXPECTATIONS FOR THE LOCAL GROUP

As the previous section showed, number counts and velocity distributions within R_v are consistent between isolated and paired MW-size haloes, but differences are evident at greater radii. In this section, we will focus on predictions in the $\sim$1 Mpc scale environment around the MW and will present results for the paired sample only.

4.1 Stellar mass functions

Although the ELVIS simulations are dissipationless, the AM technique (Kravtsov et al. 2004; Vale & Ostriker 2004; Conroy, Wechsler & Kravtsov 2006; Behroozi, Wechsler & Conroy 2013c; Moster,

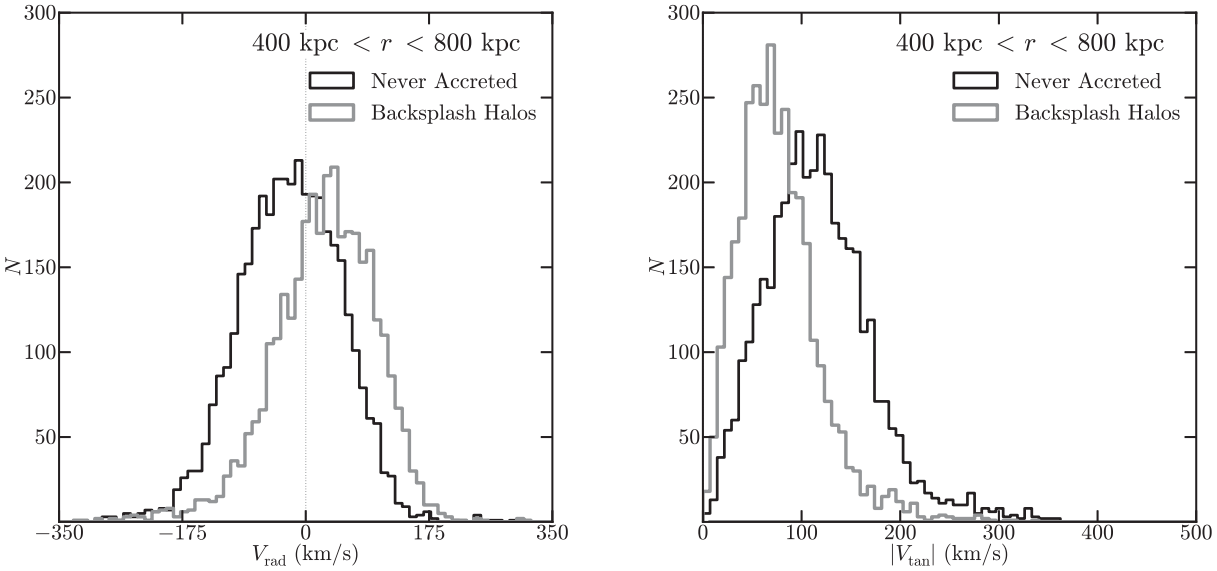

Figure 8. The radial (left) and tangential (right) velocity distributions of field haloes in the spherical shell 400–800 kpc from the centre of each paired host, truncated in the same manner as Figs 6 and 7. The black lines plot only those haloes that have never been within R_v and the grey lines includes only backsplash haloes. The latter are comparatively outflowing with relatively low tangential velocities. Note that in this figure we have excluded the two pairs in our sample with large companions at $\sim$1 Mpc distance.

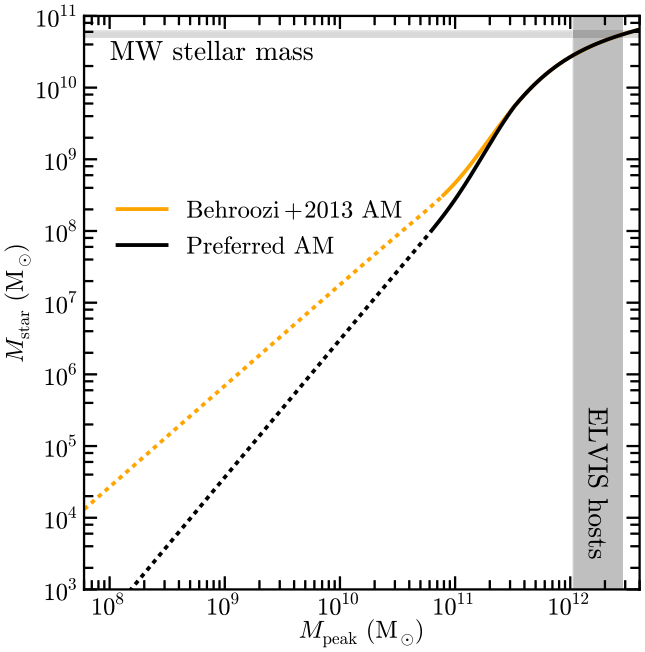

Figure 9. The AM relation between stellar mass and halo mass from Behroozi et al. (2013c, orange line), extrapolated to low halo masses, compared to a modified relation (black) motivated by the updated stellar mass function of Baldry et al. (2012). As shown in Fig. 10, this modified relation does a better job of reproducing faint ($M_* \sim 10^6$–10^8 M$_\odot$) galaxies in the LG. The two lines are solid over the range where the input stellar mass functions are complete and become dashed in the regime associated with pure extrapolation. For reference, the horizontal grey band shows the stellar mass of the MW from Bovy & Rix (2013). The virial masses of our ELVIS hosts span the vertical grey band. Note that while our halo virial masses are consistent with dynamic estimates of MW and M31 virial masses, they are at the low-mass end of AM expectations for a system with the stellar mass of the MW.

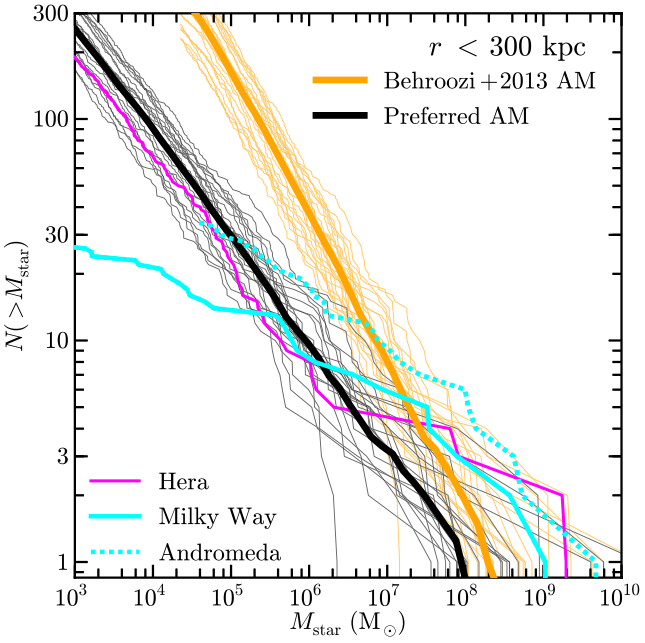

Figure 10. A comparison of observed stellar mass functions within 300 kpc of the MW (cyan) and M31 (dashed cyan) with predictions from the ELVIS subhalo catalogues and extrapolated AM relations. The orange lines use the AM prescription of Behroozi et al. (2013c), which adopts a faint-end slope of the luminosity function of −1.6 (Baldry et al. 2008), while the black curves modify the Behroozi relation by assuming a slightly shallower faint-end slope of the luminosity function of −1.47 (Baldry et al. 2012). The standard Behroozi et al. (2013c) relation overpredicts the LG data significantly at $M_* = 5 \times 10^5$ M$_\odot$, a regime where the census of satellites is believed to be complete. The modified Behroozi relation (given in the text) is a better match to the observed counts.

Naab & White 2013) makes it possible to assign stellar masses to dark matter haloes and convert the halo mass functions in Figs 3 and 5 into reasonably proxies for stellar mass functions. The connection between galaxy mass and halo mass remains highly uncertain at low masses $M_* \lesssim 10^8$ M$_\odot$, however, as it is difficult to measure luminosity functions over large volumes for dim galaxies. In this sense, comparisons to galaxy counts within the LG, where luminosity functions are more complete, can help test and refine AM relationships that have been built upon cosmological samples.

Fig. 9 shows the $z = 0$ AM relation published by Behroozi et al. (2013c) as the orange line. The plotted relation becomes dashed at $M_* < 10^{8.5}$ M$_\odot$, reflecting the approximate completeness limit of the SDSS-derived stellar mass function of Baldry, Glazebrook & Driver (2008), on which the Behroozi et al. (2013c) relation was based. The black line shows a modified version of the Behroozi et al. (2013c) relation, motivated by the updated stellar mass function of Baldry et al. (2012), who found flatter faint-end slope ($a_* = -1.47$ versus −1.6 in Baldry et al. 2008) using the Galaxy And Mass Assembly (GAMA) survey (Driver et al. 2011), which probes ∼2 mag deeper than SDSS, albeit over a smaller area of sky. In this modified relation, we have simply altered the asymptotic slope α to be 1.92 in equation 3 of Behroozi et al. (2013c), such that at small masses $M_* \propto M_{\rm peak}^{1.92}$. This is based on the expectation that $\alpha = (1 + a_{\rm dm})/(1 + a_*)$ and assuming an asymptotic halo mass function slope of $a_{\rm dm} = -1.9$ (e.g. Jenkins et al. 2001). As we show below, this modified relation does a better job in reproducing dwarf galaxy counts in the LG than the original Behroozi et al. (2013c) formulation. Our preferred relation is well described by a power law for $M_* < 10^8$ M$_\odot$:

$$M_*(M_{\rm peak}) = 3 \times 10^6\,{\rm M}_\odot \left(\frac{M_{\rm peak}}{10^{10}\,{\rm M}_\odot}\right)^{1.92}. \quad (4)$$

In the mass range of interest, this modified M_*–$M_{\rm peak}$ relation is more similar to the AM prescription presented in Moster et al. (2013). This relation is valid only at $z = 0$; our technique does not allow for a constraint at higher redshifts.

Fig. 10 shows the stellar mass functions of galaxies within 300 kpc of either the MW (cyan) or M31 (dashed cyan) compared to the predicted stellar mass functions for our ELVIS pairs based on the two AM relations shown in Fig. 9. For the galaxy stellar mass functions, we use the masses from Woo, Courteau & Dekel (2008), where available, and the luminosity data catalogued in McConnachie (2012), assuming $M_*/L = 2$, otherwise. The lines become dashed where incompleteness may become an issue (see, e.g. Koposov et al. 2008; Tollerud et al. 2008; Richardson et al. 2011; Yniguez et al. 2013).

The orange lines in Fig. 10 show the stellar mass functions for each of the 24 paired ELVIS hosts derived from the $M_*(M_{\rm peak})$ relation of Behroozi et al. (2013c). The average relation is shown by the thick line. For this exercise, we have applied the $z = 0$ relation to all subhaloes using their $M_{\rm peak}$ masses, which follows the prescription of Behroozi et al. (2013c). As can be seen, the standard Behroozi et al. (2013c) relation gives a stellar mass function that is too steep, overpredicting the count of galaxies smaller than

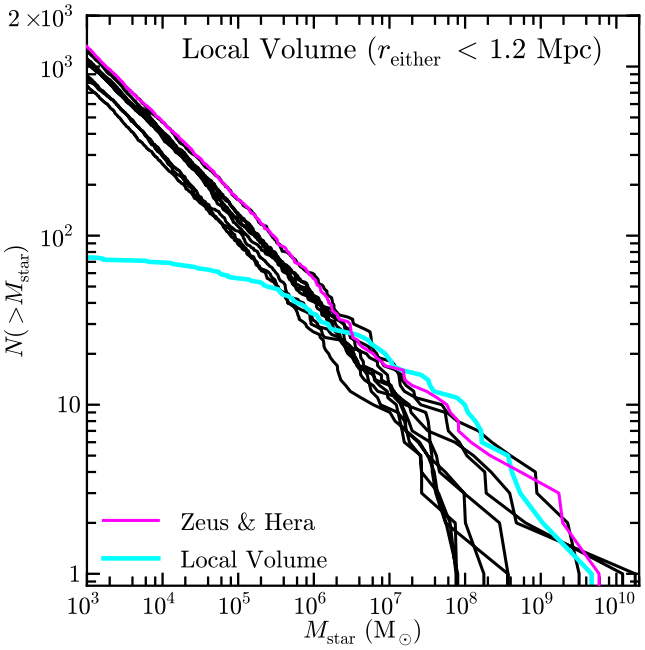

Figure 11. Cumulative stellar mass functions around paired hosts within the local volume using the preferred AM relation discussed in the text; not shown are those systems that include a third massive halo nearby (Siegfried & Roy and Serena & Venus). The pair Zeus & Hera are highlighted in magenta. The current count of galaxies within the same volume around the MW and M31 is shown in cyan (McConnachie 2012), which flattens at small mass, likely because of incompleteness. We predict ∼1000 galaxies having $M_* \geq 10^3\,{\rm M}_\odot$ within this volume, compared to the ∼70 currently known.

$M_* \simeq 10^7\,{\rm M}_\odot$ significantly. Our modified relation (applied to ELVIS haloes in black) does a better job by assigning less stellar mass to smaller haloes. For this reason, we will adopt this preferred AM relation in all relevant figures to follow. In magenta, we highlight the satellites of the host Hera, which happens to be a particularly good match to the data (at least in the regime where it is likely complete) in this and several figures that follow. Based on our preferred AM relation, we predict ∼200–300 galaxies with $M_* \geq 10^3\,{\rm M}_\odot$ within 300 kpc of the MW/M31.

We note that both AM prescriptions underpredict the satellite stellar mass function for the MW/M31 at $M_* \geq 10^8\,{\rm M}_\odot$ when considering the average satellite mass function. At these relatively high masses, however, the halo-to-halo scatter is large and the well-established rarity of LMC-like objects (Boylan-Kolchin et al. 2010; Busha et al. 2011; Tollerud et al. 2011) biases the mean result relative to observations of the LG. The stellar mass functions around individual hosts with large subhaloes, e.g. Hera in magenta, match observations well over four decades in stellar mass after applying the preferred AM relation.

Fig. 11 presents stellar mass functions for simulated local volumes (unions of 1.2 Mpc spheres around either host) using our preferred AM relation. There is one line for each pair of haloes in the ELVIS sample, excluding the two cases that contain a third large halo nearby (detailed in Section 2.3). Our AM-based prediction agrees reasonably well with the data for $M_* \gtrsim 5 \times 10^6\,{\rm M}_\odot$, but rises much more steeply towards lower masses, in the regime where the current census is almost certainly incomplete. We highlight the pair Zeus & Hera in magenta. This pair has an M_* function that happens to be very similar to that of the LG. We see that if the AM relation is extrapolated down to $M_* \sim 10^3\,{\rm M}_\odot$ we expect ∼1000 galaxies within the local volume (compared to the ∼70 systems currently known). Future surveys like those performed with LSST (Ivezic et al. 2008) will help test such extrapolations, exploring the relationship between halo mass and galaxy mass at the very threshold luminosities of galaxy formation.

4.2 H I mass functions

While future resolved star surveys promise to discover faint optical galaxies throughout the local volume, H I surveys offer a complementary approach for the discovery of dwarfs in the near-field (Blitz et al. 1999; Blitz & Robishaw 2000; Sternberg, McKee & Wolfire 2002; Adams, Giovanelli & Haynes 2013; Faerman, Sternberg & McKee 2013). While the faintest dwarfs within ∼300 kpc of either the MW or M31 are gas-poor dwarf spheroidal galaxies, gas-rich dwarfs are the norm beyond the virial regions of either giant (Grcevich & Putman 2009; McConnachie 2012). Leo T, at a distance of ∼400 kpc from the MW, is an example of a very faint system that is gas rich ($M_* \simeq M_{\rm H\,I} \simeq 10^5\,{\rm M}_\odot$; Ryan-Weber et al. 2008) and apparently falling into the MW virial radius for the first time (Rocha, Peter & Bullock 2012). Similar, though possibly even less luminous, objects may fill the local volume, and if so, could be detected in blind searches for neutral hydrogen. Recently, for example, the gas-rich galaxy Leo P ($M_{\rm H\,I} \simeq 3\,M_* \simeq 10^6\,{\rm M}_\odot$) was discovered at a distance of ∼1.5–2 Mpc using H I observations (Giovanelli et al. 2013; Rhode et al. 2013).

Here we use the ELVIS suite to provide some general expectations for the H I mass function in the local volume. Building off of the results presented in Section 4.1, we use our preferred AM relation coupled with an empirically derived $M_*-M_{\rm H\,I}$ relation to assign H I masses to haloes in our simulated local volumes. Specifically, we fit a power-law relation to the gas-rich dwarfs in the LG from McConnachie (2012), ensuring that the gas–fraction relation matches that found by Huang et al. (2012b) at higher masses:

$$M_{\rm H\,I} = 7.7 \times 10^4\,{\rm M}_\odot \left(\frac{M_*}{10^5\,{\rm M}_\odot}\right)^{1.2}. \quad (5)$$

Of course, this simple assumption of a one-to-one relation between stellar mass and H I mass is highly idealized. In reality, the gas to stellar mass relation shows a considerable amount of scatter (Kannappan 2004; McGaugh 2005; Stewart et al. 2009; Huang et al. 2012a, 2012b; Kannappan et al. 2013), and this is especially true for the faintest systems in the LG (as summarized in McConnachie 2012). A more realistic investigation of the H I content of LG galaxies is reserved for future work.

We further assume that any halo that has been within the virial radius of a giant has had all of its H I gas removed. This presupposes that a process such as ram pressure stripping removes the gas from satellites upon infall and is motivated by observations demonstrating that the vast majority of LG satellites have negligible neutral gas content (Grcevich & Putman 2009). The small number of gas-poor dwarfs that lie beyond the virial radii of either M31 or the MW (i.e. Cetus and Tucana) may very well be explained as backslash haloes (see Sales et al. 2007; Teyssier et al. 2012). Of course, some of the largest satellite galaxies in the LG (e.g. the LMC and NGC 205) are clearly able to retain H I for a non-negligible period of time after infall. This would suggest that our assumptions will lead to some undercounting of H I-rich galaxies, primarily at the highest masses. Some never accreted haloes, however, may have lost their gas via interactions with other field objects or with the cosmic web (Benítez-Llambay et al. 2013), which may lead to some overcounting at small masses.

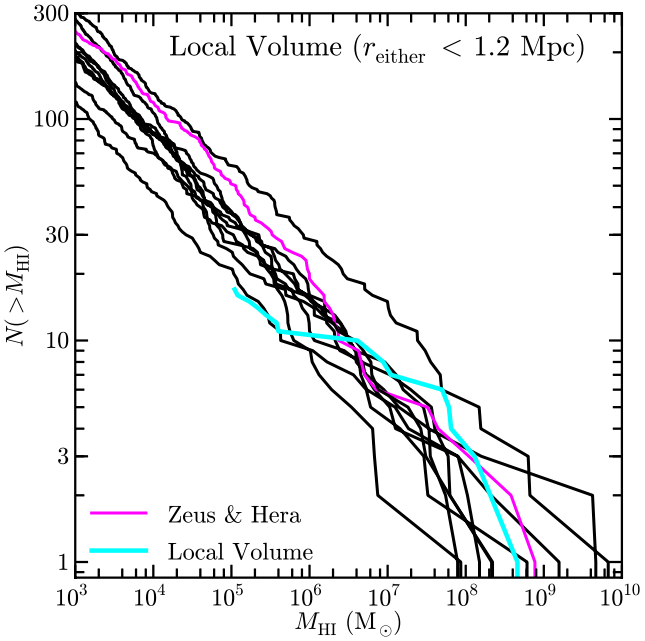

Figure 12. The H I mass functions within our simulated local volumes, excluding the systems with a third large host nearby. We assign gas masses via equation (5), assuming that any haloes that have passed within the virial radius of either giant since $z = 5$ have been stripped of all gas. The local H I mass function is consistent for $M_{\rm H\,I} \gtrsim 5 \times 10^6\,{\rm M}_\odot$; below this value, incompleteness likely sets in. We expect perhaps ∼50 undiscovered galaxies with $M_{\rm H\,I} \geq 10^5\,{\rm M}_\odot$ within 1.2 Mpc of either host.

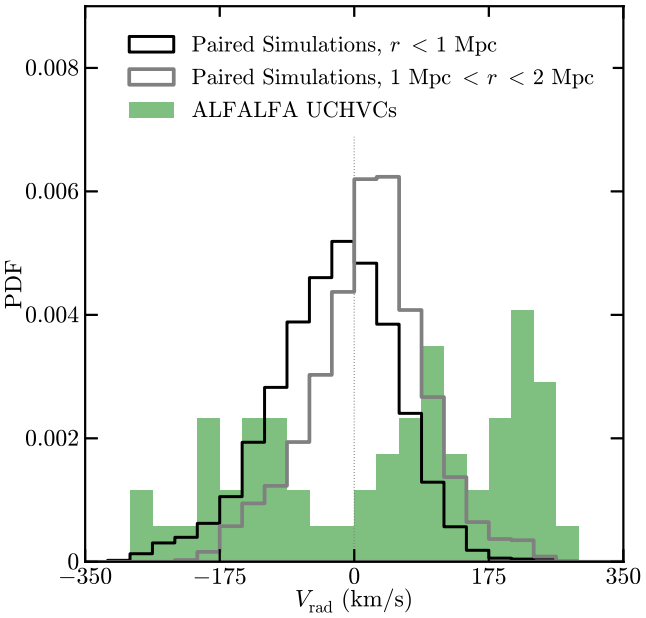

Figure 13. The black (grey) lines show the normalized radial velocity distribution of all predicted galaxies with $M_{\rm H\,I} > 10^5\,{\rm M}_\odot$ within 1 Mpc (2 Mpc) of each host. The shaded green histogram shows the radial velocities of the UCHVC halo candidates from Adams et al. (2013). While a selection bias limits the abundance of UCHVCs with $V_{\rm rad} \sim 0\,{\rm km\,s^{-1}}$, the differences at the high radial velocity tail is illuminating. Specifically, UCHVCs with $V_{\rm rad} > 175\,{\rm km\,s^{-1}}$ are highly unlikely to be associated with small haloes in the local volume according to our predictions. Systems with lower radial velocities are likely better candidates for follow up.

The predicted H I mass functions within our simulated local volumes are plotted in Fig. 12. The two systems with large interlopers have again been removed, and the line indicating Zeus & Hera is again plotted in magenta. The local H I mass function agrees well with predictions from ELVIS for $M_{\rm H\,I} \gtrsim 5 \times 10^6\,{\rm M}_\odot$, at which point the local data break sharply, likely indicating incompleteness. We estimate that there are as many as ∼50 (∼300) unidentified galaxies with $M_{\rm H\,I} \gtrsim 10^5\,{\rm M}_\odot$ ($10^3\,{\rm M}_\odot$) within 1.2 Mpc of the MW or M31.

4.3 Compact high-velocity clouds as minihaloes

It is possible that some of these gas-rich objects have already been detected. Recently, Adams et al. (2013) presented a catalogue of ultracompact high-velocity clouds (UCHVCs) extracted from the Arecibo Legacy Fast ALFA (ALFALFA; Giovanelli et al. 2005; Haynes et al. 2011) and discussed the possibility that some of these objects may be dwarf galaxies (see also Blitz et al. 1999; Faerman et al. 2013). Adams et al. (2013) present 53 candidates, with H I properties that correspond to sizes of ∼3 kpc and masses of $M_{\rm H\,I} \simeq 10^5$–$10^6\,{\rm M}_\odot$ if they reside at ∼1 Mpc distances. These characteristics are suggestively similar to those of known LG galaxies like Leo T. The ELVIS suite can be used to test whether these UCHVCs have properties (radial velocities and overall counts) that are consistent with those expected in ΛCDM for small haloes in the local volume.

From Fig. 12, we can immediately see that it is unlikely that *all* of the Adams et al. (2013) candidates are associated with small dark matter haloes in the local volume. We expect fewer than 100 undiscovered objects *over the whole sky* with $M_{\rm H\,I} \gtrsim 10^5\,{\rm M}_\odot$ within 1.2 Mpc of either host, while the ALFALFA sample has 53 candidates over only ∼10 per cent of the sky. Nevertheless, it would not be surprising if some of the identified candidates are indeed associated with dark matter dominated dwarfs.

The observed radial velocities of these clouds may provide clues for selecting the best candidates for follow-up. Fig. 13 shows the normalized stacked radial velocity distribution of $M_{\rm H\,I} > 10^5\,{\rm M}_\odot$ haloes that sit between $R_{\rm v}$ and 1 Mpc (black curve), and between 1 and 2 Mpc (grey curve) of our ELVIS pairs, measured from the centre of each host. We again exclude those objects with a third nearby giant from the black curve, and include only those objects with $R_{\rm res} > 1.75$ Mpc (Zeus, Charybdis, Romulus and Kek) in the grey curve, so as to minimize the effects of contamination from low-resolution particles. The shaded green histogram shows the radial velocity distribution of candidate minihaloes from the Adams et al. (2013) UCHVC sample. It is important to recognize that the UCHVC sample is biased to avoid the region near $V_{\rm rad} \approx 0\,{\rm km\,s^{-1}}$ by construction. Nevertheless, the high-velocity tail of distribution shows some interesting differences compared to the predicted distribution.

The most important distinction between the simulated haloes and the candidate objects is that there is a substantial population of UCHVCs with $175\,{\rm km\,s^{-1}} \lesssim V_{\rm rad} \lesssim 350\,{\rm km\,s^{-1}}$. There are very few haloes predicted with such high recessional velocities within 1 Mpc, and only slightly more out to 2 Mpc. We conclude that the subpopulation of UCHVCs with these high velocities is unlikely to be associated with dark matter haloes unless they are substantially more distant than 2 Mpc (in which case their total gas mass would become very large and thus the expected count would drop considerably). Based on these results, we suggest that targeted follow-up searches for nearby minihaloes may want to focus on UCHVC candidates with $V_{\rm rad} \lesssim 150\,{\rm km\,s^{-1}}$.

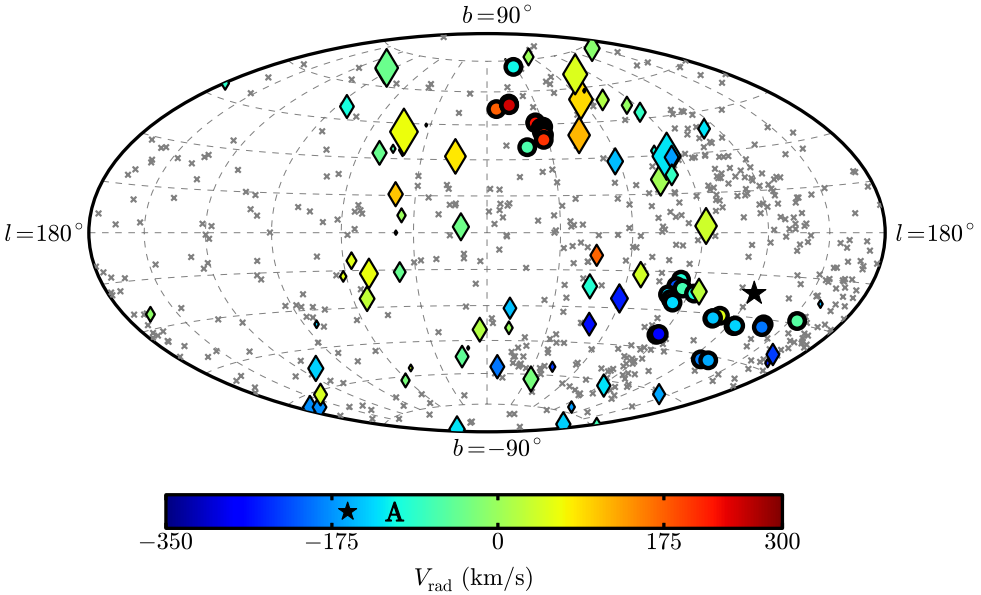

Figure 14. A Hammer projection of the haloes within 1 Mpc of Hera in mock Galactic coordinates, highlighting the haloes we expect to be gas rich with diamonds and marking backsplash haloes with crosses; no subhaloes of either giant are plotted. The simulation is rotated such that Zeus and M31 lie in the same position on the sky; this point is marked with a star. The size of the diamonds is proportional to our modelled gas mass values and distances as $\log(M_{\rm H\,I}/r^2)$. The UCHVC minihalo candidates from Adams et al. (2013) are plotted as circles with thick outlines. These and the gas-rich objects are coloured by their radial velocities according to the colour bar; the approach velocities of Zeus and Andromeda are indicated on the colour bar by the star and the A, respectively. The velocities of the fastest (outflowing) UCHVCs in the north are clearly outliers compared to the expected velocities of haloes in this region and therefore may be poor candidates for follow-up to discover dwarf galaxies. The infalling systems in the south are more in line with our kinematic expectations for minihaloes.

We also compare the on-the-sky positions of the possible minihaloes around the MW to those of the gas-rich objects near Hera, the host that we have highlighted throughout this work, in a Hammer projection in Fig. 14. The diamonds indicate the predicted galaxies around Hera and the circles denote the minihalo candidates from ALFALFA; both are coloured by their relative radial velocities according to the colour bar. We have oriented the coordinate system such that Hera's partner halo Zeus sits at the (l, b) of M31 (indicated by the star). The grey crosses are backsplash haloes. There is a clear clustering of backsplash objects near Zeus and a corresponding dearth of gas-rich haloes. Suggestively, the receding ALFALFA objects, which seem most inconsistent with the velocity distributions in ELVIS, are located near one another. We do note, however, that the gas clouds identified by ALFALFA may instead be more distant objects that are perhaps still a part of the Hubble flow. We find that most objects more than 1.5 Mpc from the centre of each host are receding.

4.4 The local $r-V_r$ relation

The velocity field within the local volume contains a wealth of information on the assembly history and mass of the LG (Kahn & Woltjer 1959; Karachentsev et al. 2002; Karachentsev 2005; Peirani & de Freitas Pacheco 2006; Teyssier et al. 2012; van der Marel et al. 2012). The ELVIS simulations supply a potentially valuable basis for interpreting these data, and we intend to utilize them for this purpose in future work. Here we briefly examine the local velocity–distance relation in one of our simulations in order to demonstrate broad agreement with data and illustrate the potential for a more in-depth interpretive analysis.

Fig. 15 shows the local relation between distance and radial velocity, centred on the LG barycenter, along with data from the Zeus & Hera simulation. MW and M31 are indicated as magenta and cyan squares, respectively, calculated from the separation and radial velocity given in Table 1 and the masses in Table 2. Known LG galaxies that reside beyond 300 kpc of either giant are shown as large diamonds; the two highlighted in yellow are the gas-free dwarfs Cetus and Tucana, which are backsplash candidates. The Leo P data point is calculated from Tables 1 and 2, assuming that its distance from the MW is 1.75 Mpc (McQuinn et al. 2013); the remainder of the observational data is taken from McConnachie (2012). For comparison, circles show all haloes within the Zeus & Hera simulation that are large enough, according to our preferred AM relation, to have stellar masses exceeding 3000 $M_\odot$. Haloes within 300 kpc of either simulated giant are excluded, but galaxies that have been within the virial radii of Zeus or Hera are coloured cyan and magenta, respectively.

As expected from the previous discussion (e.g. Fig. 8), backsplash haloes tend to populate the outflowing, positive velocity envelope of the relation. The gas-free dwarfs Cetus and Tucana are similarly consistent with inhabiting this upper envelope. More generally, the simulated relation is a reasonably good match to the data shown. The relative lack of known galaxies with $V_{\rm r} \lesssim -100\,{\rm km\,s^{-1}}$ is likely related to the barycentric velocities of the MW and M31, which are moving $\sim$50 km s^{-1} slower than Zeus and Hera.

Finally, we note that the vertical dashed line near 1.75 Mpc in Fig. 15 indicates the position of the first low-resolution (contamination) particle in the simulation. In principle, our predictions could be compromised beyond this point, but based on larger (lower resolution) simulation comparisons we find no evidence that contamination biases bulk velocity predictions.

5 CONCLUSIONS

This work presents the ELVIS suite, a set of collisionless cosmological simulations consisting of 12 LG-like pairs of

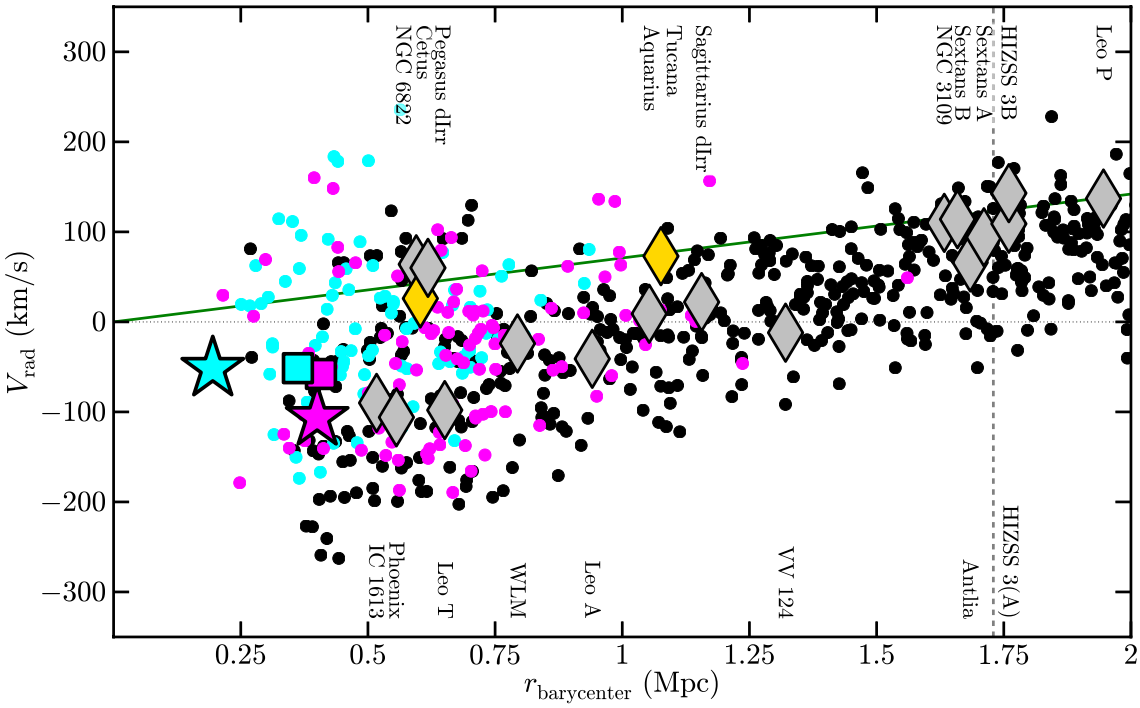

Figure 15. Barycentric radial velocity versus barycentric distance for LG galaxies compared to expectations from the Zeus & Hera simulation. The centres of Zeus (cyan) and Hera (magenta) are indicated by large stars, while M31 (cyan) and the MW (magenta) are shown by squares. All haloes with $M_* > 3 \times 10^3\,{\rm M}_\odot$ and beyond 300 kpc of either Zeus or Hera are plotted as circles. Large diamonds indicate known galaxies in the LG beyond 300 kpc of either giant. Backsplash haloes of Zeus are shown as cyan while those that have interacted with Hera are plotted in magenta. The black points are haloes that have yet to be accreted by either host. The grey diamonds mark LG galaxies that have gas while the yellow diamonds correspond to Cetus and Tucana, two gas-free dwarf that are good backslash candidates. For reference, the green line shows the asymptotic linear Hubble relation for our simulated cosmology.

MW/M31-size dark matter haloes and 24 isolated analogues mass matched to those in the pairs. Each simulation resolves minihaloes down to $M_{\rm peak} = 6 \times 10^7\,{\rm M}_\odot$ within high-resolution, contamination-free volumes that span 2 to 5 Mpc in size.

One of the goals of this work is to determine if the MW and M31 are expected to be biased in any way with respect to typical field haloes as a result of their paired configuration. We find no evidence that this is the case (cf. Fig. 3). Statistically, subhalo properties (counts and kinematics) and host halo properties (formation times and concentrations) are indistinguishable between our paired and unpaired samples. We provided analytic fits to subhalo mass functions in Section 3.1 (and for $V_{\rm max}$ functions in Appendix B). Apparently, as long as measures are restricted to the virial volumes, simulated field haloes provide an adequate comparison set for the MW and M31.

As might be expected, differences become more apparent between paired and isolated samples when we explore measures beyond the virial volumes of either hosts (Figs 4–6). The local volume at 1.2 Mpc distance around each paired host contains, on average, 80 per cent more haloes at fixed $M_{\rm peak}$ than the corresponding region surrounding each isolated host. Similarly, the kinematic properties of the minihalo population around LG-like pairs show distinct differences from isolated MWs: the tangential velocity distributions for haloes around pairs are significantly hotter, and the radial velocity distributions are skewed towards more outflowing systems. The tendency to see more outwardly moving haloes around paired hosts is likely related to another difference we see: an increase in the backsplash fraction. We find evidence that paired haloes have an increased fraction of satellite systems that are now beyond the virial radius of either host, but that had previously been inside (Fig. 7). These backsplash objects are preferentially moving outward along more radial orbits at $z = 0$ (Fig. 8).

With these basic comparisons in place, we investigate our sample of LG-like pairs more closely, focusing on comparisons with data throughout the local volume. A summary of the resultant work is as follows.

(i) We find that the AM relation presented by Behroozi et al. (2013c) overpredicts the number of $M_* \sim 5 \times 10^6\,{\rm M}_\odot$ satellites within 300 kpc of the MW and M31 (Fig. 10), a regime where the satellite census is believed to be complete.

(ii) We present a modified Behroozi relation, motivated by the stellar mass function reported by Baldry et al. (2012) from GAMA data (Fig. 9 and equation 4), that reproduces the observed satellite count down to $M_* \sim 5 \times 10^5\,{\rm M}_\odot$, a point where incompleteness likely becomes an issue. It also reproduces galaxy counts throughout the local volume down to $M_* \sim 5 \times 10^6\,{\rm M}_\odot$, below which incompleteness is almost certainly an issue (Fig. 11).

(iii) By extrapolating our preferred AM relation to low halo masses, we find there should be ∼300 galaxies with $M_* \geq 10^3\,{\rm M}_\odot$ within 300 kpc of the MW and ∼1000 such galaxies within 1.2 Mpc of either host. LSST (along with ongoing surveys) will test this expectation. If faint galaxies are not discovered in large numbers, it could point to a break in the stellar mass to halo mass relation at the low-mass end.

(iv) Using empirical relations between H I mass and stellar mass, we predict the number of gas-rich galaxies within the local volume (Fig. 12). The observed LG H I mass function agrees well with our expectations down to $M_{\rm H\,I} \sim 10^7\,{\rm M}_\odot$, below which the data may suffer from incompleteness. We conclude that there may be

approximately 50 undiscovered gas-rich haloes with $M_{\rm H\,I} > 10^5\,{\rm M}_\odot$ within 1.2 Mpc of the MW and M31.

(v) We compare the properties of our modelled gas-rich haloes to the UCHVC minihalo candidates presented by ALFALFA (Adams et al. 2013, Figs 13 and 14). While the characteristics of many of these clouds make them good candidates for gas-rich haloes, it is highly unlikely that more than ∼10 per cent are true minihaloes. In particular, positive radial velocities in excess of 175 km s^{-1} are drastically inconsistent with our expectations for halo kinematics within ∼2 Mpc of the MW.

Our results generally indicate that studies focusing on basic properties within the virial volumes of the MW or M31 can be fairly compared to predictions from more isolated field-halo simulations (e.g. Diemand et al. 2008; Kuhlen et al. 2008; Springel et al. 2008). However, simulations investigating the volume surrounding the MW *must* account for the overall environment that it lives in – specifically, the presence of the approaching M31 galaxy.

ACKNOWLEDGEMENTS

Support for this work was provided by NASA through a *Hubble Space Telescope* theory grant (programme AR-12836) from the Space Telescope Science Institute (STScI), which is operated by the Association of Universities for Research in Astronomy (AURA), Inc., under NASA contract NAS5-26555. This work was also funded in part by NSF grants AST-1009999, AST-1009973 and NASA grant NNX09AD09G. MB-K acknowledges support from the Southern California Center for Galaxy Evolution, a multicampus research programme funded by the University of California Office of Research. JSB was partially supported by the Miller Institute for Basic Research in Science during a Visiting Miller Professorship in the Department of Astronomy at the University of California Berkeley.

The authors thank Frank van den Bosch, Michael Cooper, Manoj Kaplinghat, Evan Kirby, Jose Oñorbe, Julio Navarro, Annika Peter, Risa Wechsler and Stefan Gottloeber for helpful comments, and Erik Tollerud for aid in creating the visualizations. We also thank Volker Springel for making GADGET-2 publicly available and for providing a version of GADGET-3 for our use, Peter Behroozi for making ROCKSTAR and CONSISTENT-TREES publicly available and Oliver Hahn for making MUSIC publicly available. Finally, we gratefully acknowledge the computational support of the NASA Advanced Supercomputing Division and the NASA Center for Climate Simulation, upon whose *Pleiades* and *Discover* systems these simulations were run, and the *Greenplanet* cluster at UCI, upon which much of the secondary analysis was performed.

REFERENCES

Adams E. A. K., Giovanelli R., Haynes M. P., 2013, ApJ, 768, 77
Arraki K. S., Klypin A., More S., Trujillo-Gomez S., 2012, preprint (arXiv:1212.6651)
Baldry I. K., Glazebrook K., Driver S. P., 2008, MNRAS, 388, 945
Baldry I. K. et al., 2012, MNRAS, 421, 621
Behroozi P. S., Wechsler R. H., Wu H.-Y., 2013a, ApJ, 762, 109
Behroozi P. S., Wechsler R. H., Wu H.-Y., Busha M. T., Klypin A. A., Primack J. R., 2013b, ApJ, 763, 18
Behroozi P. S., Wechsler R. H., Conroy C., 2013c, ApJ, 770, 57
Benítez-Llambay A., Navarro J. F., Abadi M. G., Gottlöber S., Yepes G., Hoffman Y., Steinmetz M., 2013, ApJ, 763, L41
Blitz L., Robishaw T., 2000, ApJ, 541, 675
Blitz L., Spergel D. N., Teuben P. J., Hartmann D., Burton W. B., 1999, ApJ, 514, 818
Boselli A., Boissier S., Cortese L., Gavazzi G., 2008, ApJ, 674, 742
Bovy J., Rix H.-W., 2013, ApJ, 779, 115
Boylan-Kolchin M., Springel V., White S. D. M., Jenkins A., Lemson G., 2009, MNRAS, 398, 1150
Boylan-Kolchin M., Springel V., White S. D. M., Jenkins A., 2010, MNRAS, 406, 896
Boylan-Kolchin M., Bullock J. S., Kaplinghat M., 2011, MNRAS, 415, L40
Boylan-Kolchin M., Bullock J. S., Kaplinghat M., 2012, MNRAS, 422, 1203
Boylan-Kolchin M., Bullock J. S., Sohn S. T., Besla G., van der Marel R. P., 2013, ApJ, 768, 140
Bryan G. L., Norman M. L., 1998, ApJ, 495, 80
Bullock J. S., Kravtsov A. V., Weinberg D. H., 2000, ApJ, 539, 517
Busha M. T., Wechsler R. H., Behroozi P. S., Gerke B. F., Klypin A. A., Primack J. R., 2011, ApJ, 743, 117
Conroy C., Wechsler R. H., Kravtsov A. V., 2006, ApJ, 647, 201
Corbelli E., 2003, MNRAS, 342, 199
Davis M., Efstathiou G., Frenk C. S., White S. D. M., 1985, ApJ, 292, 371
Diemand J., Kuhlen M., Madau P., 2007a, ApJ, 657, 262
Diemand J., Kuhlen M., Madau P., 2007b, ApJ, 667, 859
Diemand J., Kuhlen M., Madau P., Zemp M., Moore B., Potter D., Stadel J., 2008, Nature, 454, 735
Driver S. P. et al., 2011, MNRAS, 413, 971
Faerman Y., Sternberg A., McKee C. F., 2013, ApJ, 777, 119
Fardal M. A. et al., 2013, MNRAS, 434, 2779
Few C. G., Gibson B. K., Courty S., Michel-Dansac L., Brook C. B., Stinson G. S., 2012, A&A, 547, A63
Forero-Romero J. E., Hoffman Y., Yepes G., Gottlöber S., Piontek R., Klypin A., Steinmetz M., 2011, MNRAS, 417, 1434
Forero-Romero J. E., Hoffman Y., Bustamante S., Gottlöber S., Yepes G., 2013, ApJ, 767, L5
Garrison-Kimmel S., Rocha M., Boylan-Kolchin M., Bullock J. S., Lally J., 2013, MNRAS, 433, 3539
Gill S. P. D., Knebe A., Gibson B. K., 2005, MNRAS, 356, 1327
Giovanelli R. et al., 2005, AJ, 130, 2598
Giovanelli R. et al., 2013, AJ, 146, 15
Gottloeber S., Hoffman Y., Yepes G., 2010, preprint (arXiv:1005.2687)
Grcevich J., Putman M. E., 2009, ApJ, 696, 385
Gross M. A. K., Somerville R. S., Primack J. R., Holtzman J., Klypin A., 1998, MNRAS, 301, 81
Hahn O., Abel T., 2011, MNRAS, 415, 2101
Haynes M. P. et al., 2011, AJ, 142, 170
Huang S., Haynes M. P., Giovanelli R., Brinchmann J., Stierwalt S., Neff S. G., 2012a, AJ, 143, 133
Huang S., Haynes M. P., Giovanelli R., Brinchmann J., 2012b, ApJ, 756, 113
Ivezic Z. et al., 2008, preprint (arXiv:0805.2366)
Jenkins A., Frenk C. S., White S. D. M., Colberg J. M., Cole S., Evrard A. E., Couchman H. M. P., Yoshida N., 2001, MNRAS, 321, 372
Kahn F. D., Woltjer L., 1959, ApJ, 130, 705
Kannappan S. J., 2004, ApJ, 611, L89
Kannappan S. J. et al., 2013, ApJ, 777, 42
Karachentsev I. D., 2005, AJ, 129, 178
Karachentsev I. D., Kaisina E. I., 2013, AJ, 146, 46
Karachentsev I. D. et al., 2002, A&A, 389, 812
Karachentsev I. D., Karachentseva V. E., Huchtmeier W. K., Makarov D. I., 2004, AJ, 127, 2031
Katz N., White S. D. M., 1993, ApJ, 412, 455
Kawata D., Mulchaey J. S., 2008, ApJ, 672, L103
Kazantzidis S., Mayer L., Mastropietro C., Diemand J., Stadel J., Moore B., 2004, ApJ, 608, 663
Klypin A., Kravtsov A. V., Valenzuela O., Prada F., 1999, ApJ, 522, 82
Klypin A. A., Trujillo-Gomez S., Primack J., 2011, ApJ, 740, 102
Knebe A., Libeskind N. I., Doumler T., Yepes G., Gottlöber S., Hoffman Y., 2011, MNRAS, 417, L56
Knollmann S. R., Knebe A., 2009, ApJS, 182, 608
Koposov S. et al., 2008, ApJ, 686, 279

Koposov S. E., Yoo J., Rix H., Weinberg D. H., Macciò A. V., Escudé J. M., 2009, ApJ, 696, 2179
Kravtsov A. V., Berlind A. A., Wechsler R. H., Klypin A. A., Gottlöber S., Allgood B., Primack J. R., 2004, ApJ, 609, 35
Kuhlen M., Diemand J., Madau P., 2008, ApJ, 686, 262
Kuhlen M., Madau P., Silk J., 2009, Science, 325, 970
Larson D. et al., 2011, ApJS, 192, 16
Libeskind N. I., Yepes G., Knebe A., Gottlöber S., Hoffman Y., Knollmann S. R., 2010, MNRAS, 401, 1889
Li Y.-S., White S. D. M., 2008, MNRAS, 384, 1459
Madau P., Kuhlen M., Diemand J., Moore B., Zemp M., Potter D., Stadel J., 2008, ApJ, 689, L41
Makarov D., Karachentsev I., 2011, MNRAS, 412, 2498
Mamon G. A., Sanchis T., Salvador-Solé E., Solanes J. M., 2004, A&A, 414, 445
McConnachie A. W., 2012, AJ, 144, 4
McConnachie A. W., Irwin M. J., Ferguson A. M. N., Ibata R. A., Lewis G. F., Tanvir N., 2005, MNRAS, 356, 979
McGaugh S. S., 2005, ApJ, 632, 859
McQuinn K. B. W. et al., 2013, AJ, 146, 145
Miller R. H., 1964, ApJ, 140, 250
Moore B., Ghigna S., Governato F., Lake G., Quinn T., Stadel J., Tozzi P., 1999, ApJ, 524, L19
Moster B. P., Naab T., White S. D. M., 2013, MNRAS, 428, 3121
Navarro J. F., Frenk C. S., White S. D. M., 1996, ApJ, 462, 563
Olsen K. A. G., Zaritsky D., Blum R. D., Boyer M. L., Gordon K. D., 2011, ApJ, 737, 29
Oñorbe J., Garrison-Kimmel S., Maller A. H., Bullock J. S., Rocha M., Hahn O., 2014, MNRAS, 437, 1894
Peirani S., de Freitas Pacheco J. A., 2006, New Astron., 11, 325
Phillips J. I., Wheeler C., Boylan-Kolchin M., Bullock J. S., Cooper M. C., Tollerud E. J., 2014, MNRAS, 437, 1930
Piffl T. et al., 2013, preprint (arXiv:1309.4293)
Rhode K. L. et al., 2013, AJ, 145, 149
Richardson J. C. et al., 2011, ApJ, 732, 76
Ricotti M., Gnedin N. Y., 2005, ApJ, 629, 259
Rocha M., Peter A. H. G., Bullock J., 2012, MNRAS, 425, 231
Ryan-Weber E. V., Begum A., Oosterloo T., Pal S., Irwin M. J., Belokurov V., Evans N. W., Zucker D. B., 2008, MNRAS, 384, 535
Sales L. V., Navarro J. F., Abadi M. G., Steinmetz M., 2007, MNRAS, 379, 1475
Springel V., 2005, MNRAS, 364, 1105
Springel V. et al., 2005, Nature, 435, 629
Springel V. et al., 2008, MNRAS, 391, 1685
Sternberg A., McKee C. F., Wolfire M. G., 2002, ApJS, 143, 419
Stewart K. R., Bullock J. S., Wechsler R. H., Maller A. H., 2009, ApJ, 702, 307
Strigari L. E., Bullock J. S., Kaplinghat M., Simon J. D., Geha M., Willman B., Walker M. G., 2008, Nature, 454, 1096
Strigari L. E., Frenk C. S., White S. D. M., 2010, MNRAS, 408, 2364
Teyssier M., Johnston K. V., Kuhlen M., 2012, MNRAS, 426, 1808
Tikhonov A. V., Klypin A., 2009, MNRAS, 395, 1915
Tollerud E. J., Bullock J. S., Strigari L. E., Willman B., 2008, ApJ, 688, 277
Tollerud E. J., Barton E. J., Bullock J. S., Trinh C., 2011, in Koleva M., Prugniel P., Vauglin I., eds, EAS Publ. Ser., Vol. 48, p. 455
Tollerud E. J. et al., 2012, ApJ, 752, 45
Tully R. B. et al., 2013, AJ, 146, 86
Vale A., Ostriker J. P., 2004, MNRAS, 353, 189
van der Marel R. P., Fardal M., Besla G., Beaton R. L., Sohn S. T., Anderson J., Brown T., Guhathakurta P., 2012, ApJ, 753, 8
Walker M. G., Peñarrubia J., 2011, ApJ, 742, 20
Weisz D. R. et al., 2011, ApJ, 743, 8
Woo J., Courteau S., Dekel A., 2008, MNRAS, 390, 1453
Woo J. et al., 2013, MNRAS, 428, 3306
Wu H.-Y., Hahn O., Wechsler R. H., Behroozi P. S., Mao Y.-Y., 2013, ApJ, 767, 23
Yniguez B., Garrison-Kimmel S., Boylan-Kolchin M., Bullock J. S., 2013, preprint (arXiv:1305.0560)
Zentner A. R., Bullock J. S., 2003, ApJ, 598, 49
Zolotov A. et al., 2012, ApJ, 761, 71

APPENDIX A: NUMERICAL CONVERGENCE

In this appendix, we compare the $M_{\rm peak}$ and $V_{\rm max}$ functions within 400 kpc of iKauket at three different levels of numerical resolution. Fig. A1 contains this comparison: results from the HiRes simulation ($m_{\rm p} = 2.35 \times 10^4\,{\rm M}_\odot$, $\epsilon = 70.4\,{\rm pc}$) are shown as a red

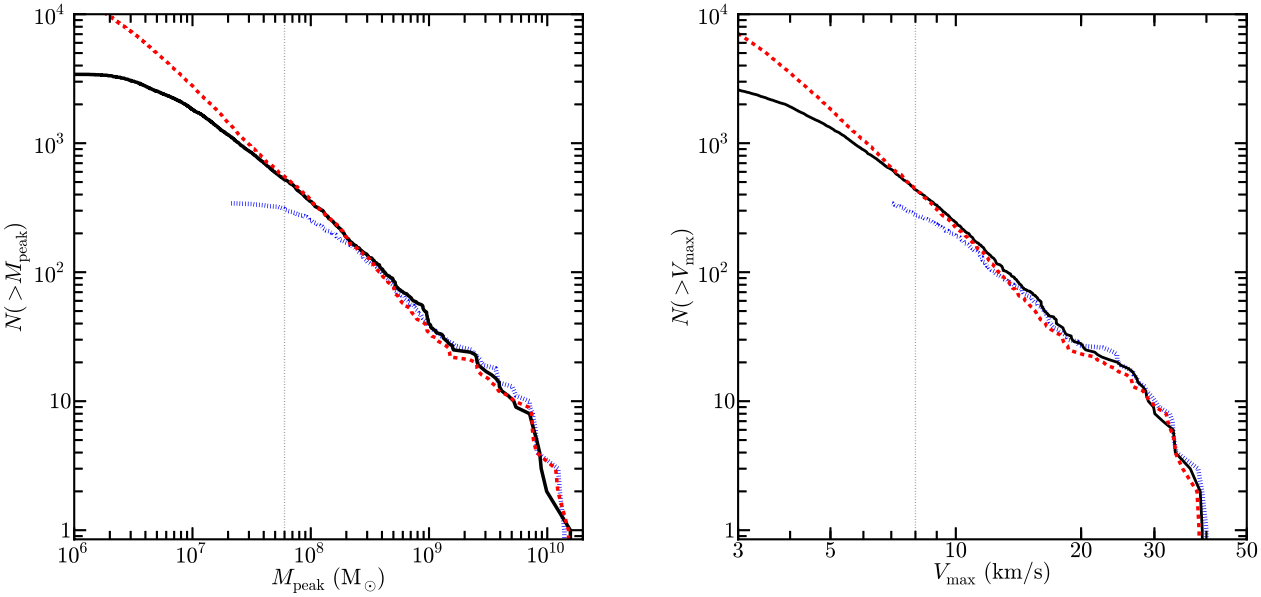

Figure A1. Resolution test indicating the smallest haloes ROCKSTAR reliably identifies in the ELVIS simulations. Here we plot the $M_{\rm peak}$ (left) and $V_{\rm max}$ (right) functions for haloes within 400 kpc of the smallest of our isolated haloes, iKauket. The black line indicates the fiducial resolution; the red line is from the HiRes simulation, and the blue line is from a lower resolution run, for illustrative purposes. The mass and circular velocity at which the lines begin to systematically disagree, $M_{\rm peak} = 6 \times 10^7\,{\rm M}_\odot$ and $V_{\rm max} = 8\,{\rm km\,s^{-1}}$, constitute our resolution limits for the fiducial resolution.

dashed line, while results from the run at our fiducial resolution ($m_p = 1.89 \times 10^5\,M_\odot$, $\epsilon = 141$ pc) are shown as a solid black line. For comparison, the blue line shows a lower resolution run as well ($m_p = 1.55 \times 10^6\,M_\odot$, $\epsilon = 469$ pc).

The left-hand panel plots the number of haloes identified by our pipeline with M_{peak} greater than a given mass; on the right, we plot the current V_{max} function. By locating where our fiducial resolution begins to systematically differ from the HiRes run, it is clear that haloes with $V_{max} > 8\,km\,s^{-1}$ and $M_{peak} > 6 \times 10^7\,M_\odot$ are reliably identified at the fiducial resolution. These resolution limits are marked by dashed vertical lines in the plots.

APPENDIX B: V_{max} FUNCTIONS

For most galaxies, it is more convenient to measure circular velocities or velocity dispersions than virial mass. Although we do show stellar mass functions in the main body, our relation is not a mapping between M_* and V_{max}; thus, we show V_{max} functions for direct comparison with such observations here. As with the M_{peak} functions, counts as a function of V_{max} agree well within R_v (Fig. B1), and are both well fitted by a power law at the low-mass end:

$$N_v(>V_{max}/V_v) = 0.038(V_{max}/V_v)^{-3.3}.$$

The V_{max} function in the local fields is also similarly offset (Fig. B2), with the paired simulations lying 75 per cent higher than the isolated analogues:

$$N_{0.3-1}(>V_{max}) = N_0 \left(\frac{V_{max}}{10\,km\,s^{-1}}\right)^{-3.1},$$

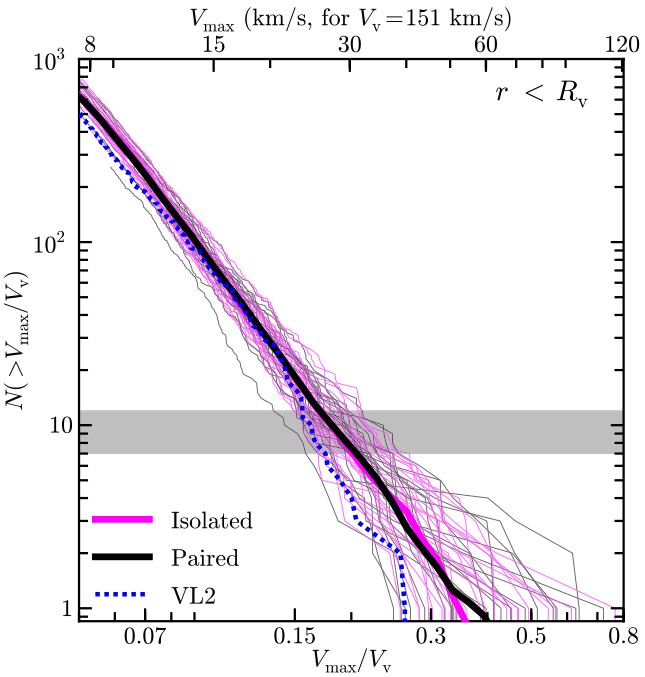

Figure B1. The V_{max} function within R_v of each host, scaled by the virial velocity of that host, analogous to Fig. 3. As in that figure, the two populations agree well within the virial radius and are both well fitted at the low-mass end by a power law of slope −3.1, as given in the text. The blue dashed line plots the V_{max} function within the virial radius of the high-resolution Via Lactea II halo (Kuhlen, Madau & Silk 2009), which agrees within the halo-to-halo scatter.

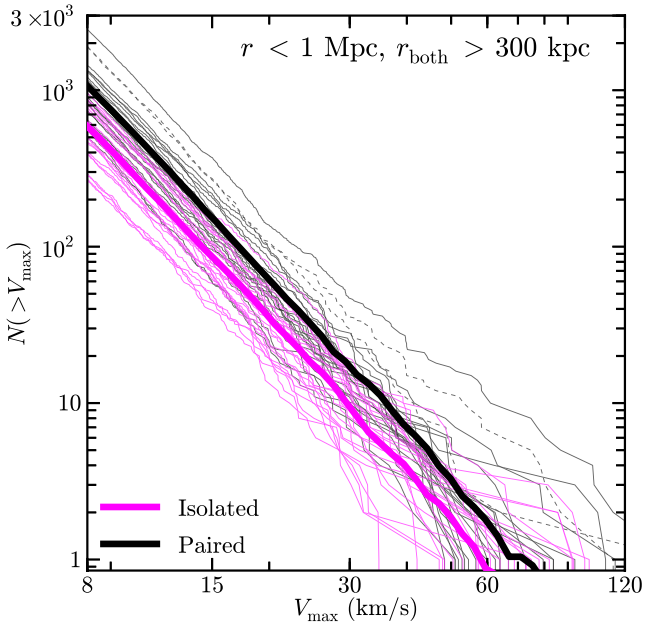

Figure B2. The V_{max} functions for objects in the local field (within 1 Mpc of the host, but more than 300 pc from both giants). The average relations are offset from one another, with the paired simulations having an amplitude that is 75 per cent higher. The power-law fits to the average relations are given in the text.

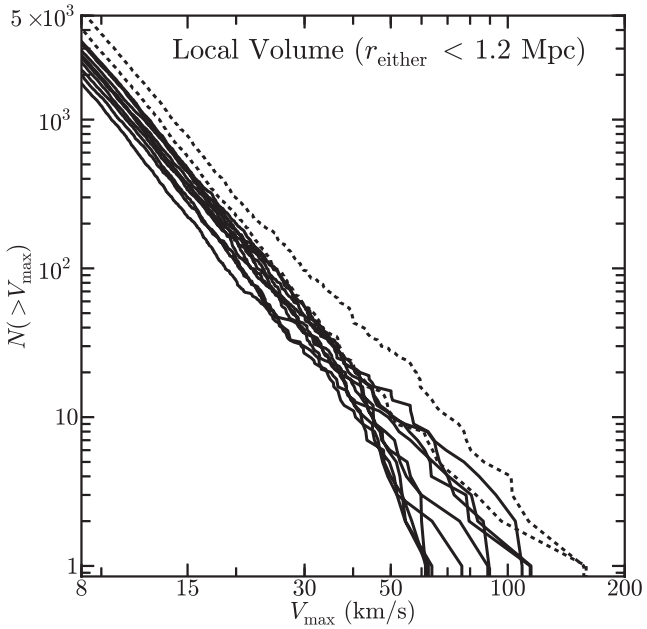

Figure B3. The V_{max} functions in the local volume (1.2 Mpc of either host), analogous to Fig. 5.

with $N_0 = 540$ for the paired sample and 300 for the isolated analogues. Likewise, we predict similar numbers of objects with $V_{max} > 8\,km\,s^{-1}$ within the 1 Mpc of each host and within the local volume around each pair as predicted in Fig. 5 for $M_{peak} > 6 \times 10^7\,M_\odot$; these V_{max} functions are plotted in Fig. B3.

This paper has been typeset from a TEX/LATEX file prepared by the author.